

CAVITY, Calar Alto Void Integral-field Treasury survey and project extension

I. Pérez^{1,2}, S. Verley^{1,2}, L. Sánchez-Menguiano^{1,2}, T. Ruiz-Lara^{1,2}, R. García-Benito³, S. Duarte Puertas^{1,2,4}, A. Jiménez¹, J. Domínguez-Gómez¹, D. Espada^{1,2}, R. F. Peletier⁵, J. Román^{6,7}, M. I. Rodríguez¹, P. Sánchez Alarcón⁶, M. Argudo-Fernández^{1,2}, G. Torres-Ríos¹, B. Bidaran¹, M. Alcázar-Layne¹, R. van de Weygaert⁵, S.F. Sánchez⁸, U. Lisenfeld^{1,2}, A. Zurita^{1,2}, E. Florido^{1,2}, J.M. van der Hulst⁵, G. Blázquez-Calero³, P. Villalba-González⁹, I. del Moral-Castro¹⁰, A. Lugo-Aranda¹¹, D. Walo-Martín⁶, A. Conrado³, R. González-Delgado³, J. Falcón-Barroso^{6,7}, A. Ferré-Mateu^{6,7}, M. Hernández-Sánchez¹², P. Awad^{5,13}, K. Kreckel¹⁴, H. Courtois¹⁵, R. Espada-Miura¹, M. Relaño^{1,2}, L. Galbany¹⁶, P. Sánchez-Blázquez¹⁷, E. Pérez-Montero³, M. Sánchez-Portal¹⁸, A. Bongiovanni¹⁸, S. Planelles¹², V. Quilis¹², M. Aubert¹⁵, D. Guinet¹⁵, D. Pomarède¹⁵, A. Weijmans¹⁹, M. A. Raj⁵, J. Aragón-Calvo⁸, M. Azzaro²⁰, G. Bergond²⁰, M. Blazek²⁰, S. Cikota²⁰, A. Fernández-Martín²⁰, A. Gardini²⁰, A. Guijarro²⁰, I. Hermelo²⁰, P. Martín²⁰, and I. Vico²⁰

(Affiliations can be found after the references)

Received — / Accepted —

ABSTRACT

We have learnt in the last decades that the majority of galaxies belong to high density regions interconnected in a sponge-like fashion. This large-scale structure is characterised by clusters, filaments, walls, where most galaxies concentrate, but also under-dense regions, called voids. The void regions and the galaxies within represent an ideal place for the study of galaxy formation and evolution as they are largely unaffected by the complex physical processes that transform galaxies in high-density environments. These void galaxies can hold the key as well to answer current challenges to the Λ CDM paradigm. The Calar Alto Void Integral-field Treasury survey (CAVITY) is a Legacy project approved by the Calar Alto Observatory to obtain spatially resolved spectroscopic information of ~ 300 void galaxies in the Local Universe ($0.005 < z < 0.050$) covering from -17.0 to -21.5 in r band absolute magnitude. It officially started in January 2021 and has been awarded 110 useful dark observing nights at the 3.5 m telescope using the PMAS spectrograph. Complementary follow-up projects including deep optical imaging, integrated, as well as resolved CO data, and integrated HI spectra, have joint the PMAS observations and naturally complete the scientific aim of characterising galaxies in cosmic voids. The extension data has been denominated CAVITY+. The data will be available to the whole community in different data releases, the first of which is planned for July 2024, and it will provide the community with PMAS data cubes for around 100 void galaxies through a user friendly, and well documented, database platform. We present here the survey, sample selection, data reduction, quality control schemes, science goals, and some examples of the scientific power of the CAVITY and CAVITY+ data.

Key words. Surveys – large-scale structure of Universe – Galaxies: evolution – Galaxies: formation – Techniques: imaging spectroscopy

1. Introduction

Galaxies are not uniformly distributed throughout space at large scales, that is, at scales larger than 10 Mpc. Instead, they form a foam-like structure characterised by elongated filaments, sheet-like walls, dense clusters, and under-dense regions in between called voids. These voids are an integral part of the cosmic web (see e.g. van de Weygaert & Platen 2011, for a review), representing around 70% of the Universe volume, but they only host around 10% of the mass (Libeskind et al. 2018). Voids appear from the primordial Gaussian field of density fluctuations, and as a result of their under-density, they represent regions of weaker gravity, and therefore growing faster than the Hubble flow. As they expand, matter is pushed in between them into the filaments and sheets that contract faster by their own gravity.

In a seminal work, Cautun et al. (2014) showed from the analysis of dark-matter only numerical cosmological simulations the complex evolution of the Universe structures. These show substructures as part of the hierarchical nature of the cosmic web. This complexity poses a challenge when trying to identify the cosmic web patterns. The halo mass distribution function of

voids is populated by low mass objects as compared to the halo mass distribution of walls, filaments, and clusters. As the Universe evolves, the lowest density regions tend to expand and become even emptier, as matter seems to flow from the low density regions to the denser environments, and therefore, the dynamical stage of the void can tell us the story of its formation and future fate.

Voids then represent the key to the arrangement of the large scale structure of the cosmic web. Despite their name, void structures contain galaxies. These void galaxies, as they evolve in a low density Universe show more recent star formation as compared to galaxies in denser environments (as suggested by some works, e.g. Lackner et al. 2012), provide clues on how halos assemble their mass in the early Universe and can help us to understand the time when internal mechanisms take over in galaxy evolution, and how they depend on the large scale structure.

We know that galaxies in the Universe come broadly in two general flavours: galaxies that are forming stars, and galaxies that are quiescent. The physical mechanisms that transform star-forming galaxies into quiescent passive systems are still unclear in spite that it is a key stage in galaxy evolution. Some mecha-

nisms have been proposed: outflows to remove the gas (Di Matteo et al. 2005; Hopkins et al. 2006; Maiolino et al. 2012), stripping of the gas (e.g. Quilis et al. 2000), or strangulation (e.g. Dekel & Cox 2006). It is also well established that galaxy interactions can cause an enhancement of the star formation rate (e.g. Larson & Tinsley 1978; Brassington et al. 2015; Knapen & Cisternas 2015), the largest enhancement occurring in equal-mass mergers after the first pericenter passage and, much stronger, during coalescence (e.g. Nikolic et al. 2004; Scudder et al. 2012). Void galaxies reside in environments that are largely unaffected by the processes modifying galaxies in denser environments and this should reflect on their star formation histories (SFHs). By removing the physical processes of dense environments we are left studying a ‘simplified’, pristine environment that can help us to understand what are the main drivers of galaxy transformation. Observations seem to indicate that void galaxies are similar to galaxies in denser regions although they tend to be bluer and of later type morphologies than galaxies in denser environments (e.g. Rojas et al. 2004, 2005; Park et al. 2007; Constantin et al. 2008). Some works show indications that the specific star formation rate ($sSFR = SFR/M_*$) of void galaxies might be slightly enhanced with respect to non-void galaxies (Beygu et al. 2017), but the works are inconclusive. Recent results (Domínguez-Gómez et al. 2022), for a sample of 20 void galaxies, hint towards some differences between the star formation efficiency (SFE) of void and non-void galaxies, excluding those in clusters. They also showed that the molecular content seems to be similar, although a larger sample is necessary to confirm the trends.

It is becoming more and more clear that the environment has an influence on the stellar mass of the galaxies, as void galaxies do not seem to follow the morphology-density relation (Dressler 1980), lacking very low mass galaxies, $M_* < 10^7 M_\odot$ (van de Weygaert et al. 2011; Beygu et al. 2016). There are discrepancies about the present metallicity content of the gas in void galaxies. Some studies show systematic lower metallicities (Pustilnik & Tepliakova 2011). However, a study of luminous void galaxies shows no deviation from the standard mass-metallicity relation (Kreckel et al. 2015). With integral field spectroscopy (IFS) data, we can directly measure the metallicity gradient and determine the metallicity at a fixed galaxy effective radius. Furthermore, given the evidence for ongoing cold accretion of pristine material in some void galaxies (Stanonik et al. 2009), this could be identifiable as asymmetries in 2D metallicity maps.

Observationally, the controversy remains, however, as to whether or not the properties, including the mass of the dark halo, of galaxies in voids differ from comparable objects in walls and filaments. Some of the controversy could be due to a lack of a proper characterisation of the void substructure and the void dynamical stage. Furthermore, all these studies lack a view on how star formation occurred in the past and when and how the mass was put together. SFHs, including the run of star formation with time and the cosmic chemical enrichment of stars hold the key to understand the baryonic mass assembly of galaxies in these low density environments. What we observe in galaxies is the accumulated history of generations and generations of stars. The properties of the stars currently located in a galaxy reflect the different episodes of star formation and the interstellar medium enrichment processes undergone. Therefore, by deriving the current stellar composition in galaxies we can trace back the history of how stars have been formed over the entire evolution of the galaxy, i.e. we can obtain its SFH. Indeed, in a recent study, carried out on the Sloan Digital Sky Survey (SDSS) spectra of a well defined sample of void, wall/filament, cluster galaxies, defined as the CAVITY parent sample (see Sect. 3)

we concluded that the stellar mass assembly of void galaxies occurs slower than in denser environments (Domínguez-Gómez et al. 2023b). On the analysis of stellar metallicities of the same sample, Domínguez-Gómez et al. (2023a) found that, on average, void galaxies have lower stellar metallicities than galaxies in denser environments.

It has been previously shown that spatially resolved SFHs of galaxies, obtained from IFS data, can determine the epoch of galaxy structure formation (e.g. García-Benito et al. 2017; Pérez et al. 2017). In addition, previous studies have demonstrated that deriving SFHs from integrated spectra using full spectral fitting techniques provides robust results as compared to resolved stellar populations (e.g. García-Benito & Pérez-Montero 2012; Ruiz-Lara et al. 2015, 2018b).

All these facts make the time ripe for a detailed, and spatially resolved study of baryonic mass assembly in the most underdense regions of the cosmic web, motivating the development of the CAVITY project, presented in this work.

In Sect. 2 we present an outline of the CAVITY project. Sect. 3 describes the void and galaxy selection that conforms the CAVITY parent sample. In Sect. 4 we detail the on-going observation strategy and data reduction pipeline. Sect. 5 outlines the quality assessment performed on the IFS data. In Sect. 6 we describe in detail the project extension, named as CAVITY+. We explain here the generalities of the CO, HI and deep optical imaging data. In Sect. 7 we present the main project goals and some examples of the scientific power of the CAVITY and CAVITY+ data.

2. CAVITY project summary

Calar Alto Void Integral-field Treasury survey (CAVITY) is a survey aimed to study galaxies in voids using IFS data. The project was approved in 2020 by the Calar Alto Observatory (CAHA, Spain) as a Legacy project, being awarded 110 useful observing nights at the 3.5 m telescope using the PMAS spectrograph. The observatory officially started scheduling CAVITY nights in January 2021.

CAVITY is currently addressing in detail the previously discussed issues on SFHs, and the physical properties of the ionised gas. Furthermore, the dark mass content of these galaxies is also of high interest for the project. Since the relation between the baryonic mass and its dark halo is not linear (e.g. Moster et al. 2013), in order to assess the whole galaxy assembling we need to first determine the dark matter contribution to the whole potential. We will be able to address the dark content of void galaxies with the IFS data. Observationally, determining the dark mass of void galaxies has been attempted on a sample of void galaxies present in the MaNGA catalogue (Douglass et al. 2019) finding no significant difference between galaxies located in voids and in denser environments. The CAVITY sample (see Sect. 3) has been specifically designed to study galaxies within voids, as well as sampling voids of different sizes, and at different dynamical stages. The CAVITY project will also address the predictions of the current cosmological model, the Λ CDM model, for the mass assembling of galaxies in different environments. The Λ CDM model, which is the parametrisation of the Big-Bang theory with dark matter and dark energy, has been very successful at predicting the main observables in the Universe (large-scale structure, cosmic microwave background, acceleration of the expansion of the Universe, and the abundances of elements). However, it still fails at predicting the scales at which baryon physics dominates, i.e. galaxy scale (e.g. Simon & Geha 2007; Klypin et al. 2009). The details of the time-scales at which baryons assembled

to form galaxies in the early Universe, and their relation with their hosting dark halo still remains controversial as the baryon physics is difficult to model. CAVITY will serve as the perfect benchmark to confront the state-of-the-art numerical predictions from Λ CDM, which will help us interpret the general context of voids in the formation and evolution of galaxies.

Summarising, CAVITY is a spatially resolved survey of void galaxies aiming to: 1) determine how the large-scale environment has influenced the mass assembly of void galaxies; 2) establish how galaxy formation and its properties are dependent on the large scale-environment; 3) find the main drivers for galaxy transformation; and 4) determine the dark matter content of void galaxies. Figure 1 illustrates the CAVITY project and its unparalleled power to characterise galaxies in voids.

The IFS data for the first 100 galaxies will be made completely available to the public as part of the first CAVITY Data Release (DR1) through an easy access database planned for July 2024. The full sample and high-level data products are planned to be released by 2025/2026.

3. Sample selection and characterisation

A broad definition of a cosmic void as a large under-dense (average density contrast of about -0.9) structure of diameters generally between 20 to 100 Mpc is a clearly accepted one (e.g. Platen et al. 2008). However, when it comes to the details of determining the shape of a void and its limits within the large scale structure, in both galaxy surveys and simulations, it becomes a tricky task which is subject to different detection algorithms that present clear differences among each other but they agree in the generalities (e.g. Colberg et al. 2008; Libeskind et al. 2018). Overall, most void finder strategies in survey data use a conversion from redshift to 3D distance and then estimate a local density field from either the raw or smoothed data, assuming or not some shape priors. Many void finders assume approximately spherical voids (Hoyle & Vogeley 2002), or sum of spheres or “holes” (e.g. Hoyle & Vogeley 2004; Pan et al. 2012), while others base their catalogues in void-finder codes that make no assumption on the shape of voids, using some tessellation technique to obtain the density field and a ‘watershed’ threshold (e.g. Nadathur & Hotchkiss 2014; Sutter et al. 2015). These void identifications have to take into account that some voids may also show internal substructure known as “tendrils” (El-Ad & Piran 1997; Hoyle & Vogeley 2002, 2004).

Once cosmic voids have been identified, one can start identifying galaxies inhabiting these voids. In the nearby Universe ($z < 0.1$), several void catalogues have been produced from the SDSS data (Pan et al. 2012; Nadathur & Hotchkiss 2014; Douglass et al. 2022). For the selection of CAVITY galaxies we opted to use the Pan et al. (2012) catalogue based on SDSS data, which is a well characterised catalogue of nearby voids. We have restricted ourselves to voids in the catalogue where the full volume of the void is included in the SDSS footprint within the redshift range 0.005 and 0.050, these redshift limits also allow us to obtain a full volume coverage of voids of large sizes. In addition, we have selected galaxies with intermediate inclinations, with a final inclination distribution between 20 and 70 degrees, visually discarding a few very edge- and face-on systems, where the intermediate inclinations derived from LEDA¹ (Makarov et al. 2014) and SDSS² (Abazajian et al. 2009) were clearly wrongly estimated. From the initial 79947 galaxies in the sample of 1055

voids in Pan et al. (2012), we are left with 19857 in 96 voids that fulfil the criteria of the redshift range and fitting the full void within the SDSS footprint. To accurately characterise voids, we establish a criterion requiring at least 20 galaxies per void. This results in a total of 19,732 galaxies distributed across 80 voids. After removing the voids at the edges of the SDSS footprint, where possibly part of the void volume is missing, we are left with 8690 galaxies in 42 voids. From these 42 voids we have selected 15 representative voids to cover the full ranges in void effective radius, volume number densities, number of galaxies within voids, and right ascension, to maximise the observability from the Calar Alto Observatory. The selection also ensures that the distribution of some properties of the galaxies within the 15 voids are representative of those within the 42 voids, such as redshift, effective radius fraction, R_{90} Petrosian, R absolute magnitude, $g - r$ colour distributions. This later selection leaves us with a sample of 4866 galaxies, which is considered the CAVITY parent sample. From these, we have removed those objects in common with the cluster catalogue of Tempel et al. (2017) to ensure that we had no galaxies in the sample belonging to clusters.

As previously discussed, the membership of a particular galaxy to a void structure or to a higher density environment is a decision dependent on the void detection algorithm used. This is more evident at the edges of the structures. To ensure that the final selection is basically dominated by void galaxies we have imposed an extra selection criterion based on the distance of the galaxy to the centre of the void, characterised by the effective radius parameter (R_{eff}) that corresponds to the radius of a spherical void of equal volume. This is a simplification, since we know that the intrinsic shape of voids is more complex than a simple spherical representation (Neyrinck 2008; Sutter et al. 2015). A galaxy needs to be within a radius of $0.8 \times R_{\text{eff}}$, with the R_{eff} as defined above, to be included in the sample.

During the sample selection phase we developed a hybrid approach mixing information from well-known catalogues (LEDA and SDSS) as well as a visual inspection (using GALAssify, Alcázar-Laynez et al. 2024, in prep.) to revise the sample and discard galaxies that have too bright stars in the PMAS FoV, very edge-on systems (as described before), and galaxies that show too low surface brightness to be observed with PMAS (below an average μ_r of 25 mag arcsec²). After this process, we are left with 1115 observable galaxies. From these 1115 galaxies, 44 of them are included in the MaNGA sample (Bundy et al. 2015) and one galaxy is in common with the CALIFA survey (Sánchez et al. 2012). The top and bottom panels of Fig. 2 show the Colour-Magnitude diagram and the distribution of center-void distances within the void (normalised to the void R_{eff}) of the final observable sample, respectively.

4. Observation strategy and data reduction

Observations are performed with the Postdam Multi Aperture Spectrograph (PMAS, Roth et al. 2005) in the PPak mode (Kelz et al. 2006). The PPak fibre bundle consists of 382 fibres of 2.68 arcsec diameter each. The science bundle is comprised of 331 fibres in an hexagonal configuration covering a FoV of $74'' \times 64''$, with a filling factor of $\sim 60\%$. Six independent fibre bundles of 6 fibres each conform the sky background sampling. These bundles are distributed along a circle at ~ 72 arcsec from the centre of the instrument FoV (see Fig. 5 of Kelz et al. 2006, for an overall layout of the PPak IFS). Finally, there are 15 extra calibration fibres which are not part of the IFS, that can be illuminated with the light from the spectral-line lamps during science exposures.

¹ <http://leda.univ-lyon1.fr/>

² <https://classic.sdss.org/dr7/>

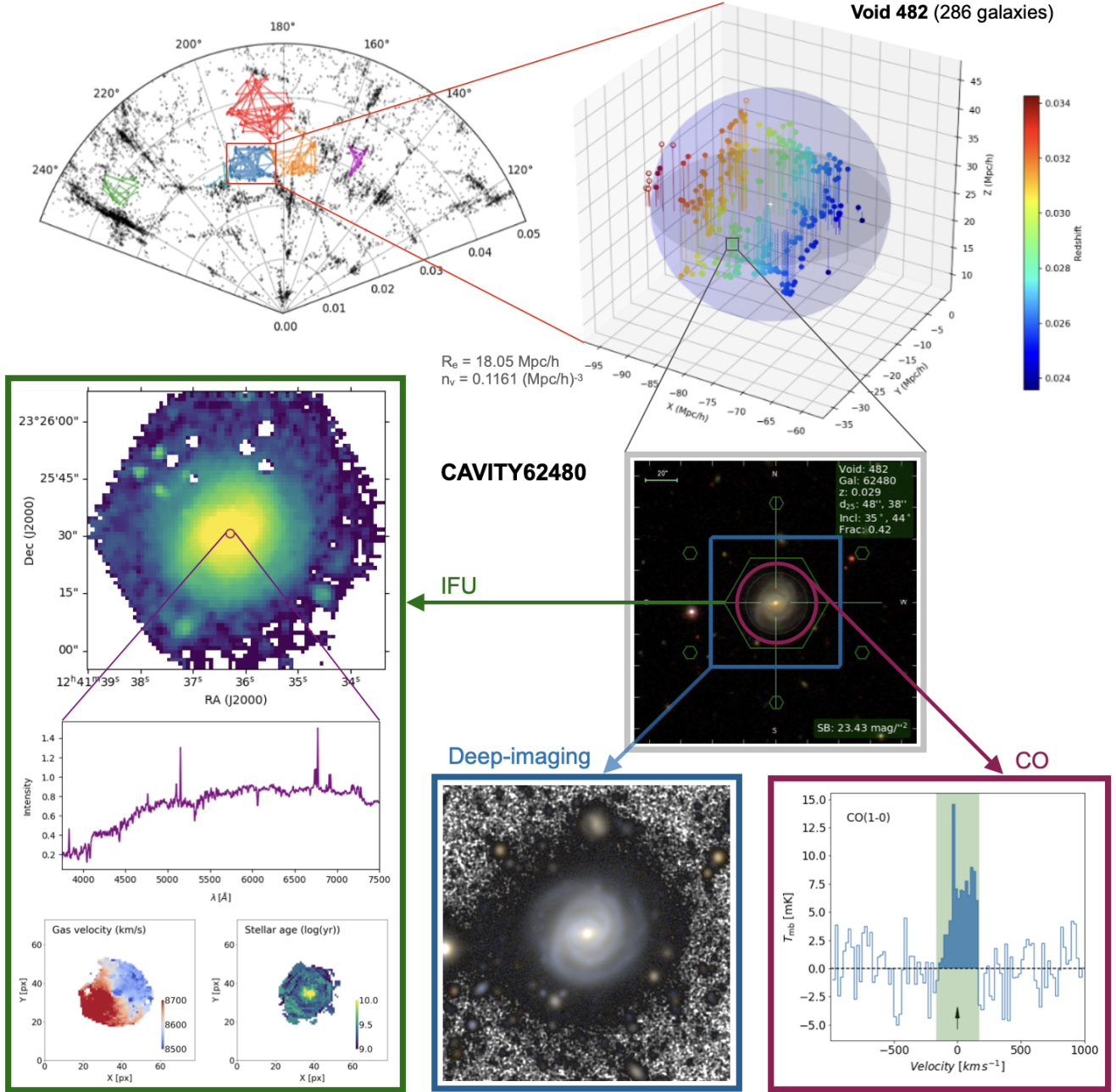


Fig. 1. This figure is divided into three main sections. At the top we illustrate some randomly-selected CAVITY voids within the large-scale structure of the Universe (as a wedge plot on the left, [Argudo-Fernández et al. \(2017\)](#)) as well as show the spatial distribution of galaxies within a typical void (void 486, each dot corresponding to a different galaxy colour-coded by redshift). The webs of colour lines link galaxy members and depict the location of each highlighted void. The middle right panel (framed by a grey square) zooms in on CAVITY62480, an example galaxy contained in void 482, showing its SDSS colour image with the PMAS footprint (green hexagon), INT cutout (blue square) and IRAM beam (purple circle) on top of it. The next main section (framed by the green rectangle) is devoted to illustrate the IFS data. We represent the integrated light of the galaxy within the covered wavelength range of the instrument (on top), the spectrum of the central spaxel (in the middle), and the gas velocity and stellar age maps (at the bottom) as examples of the potential of IFS data in deriving spatially-resolved distributions of the galaxy properties. The third and final section is devoted to CAVITY+, the complementary observational campaigns that shape the CAVITY project extension. Here we show a coloured image using the INT g- and r-band deep imaging (framed by the blue rectangle, bottom middle panel) and the integrated CO(1-0) spectrum from the IRAM observations (purple rectangle, bottom right panel) for CAVITY62480.

Observations are carried out using the V500 grating. This grating has a nominal resolution of $\lambda/\Delta\lambda \approx 850$ at $\sim 5000 \text{ \AA}$ with a full width at half maximum (FWHM) of about 6 \AA , covering from 3745 to 7300 \AA and thus including from $[\text{OII}]\lambda 3727$ to $[\text{SII}]\lambda 6731$ in rest-frame of all galaxies of the survey. The brightest and largest objects of the sample, around 50%, will also be

observed using grating V1200. This grating has a nominal resolution of $\lambda/\Delta\lambda \approx 1650$ at $\sim 4500 \text{ \AA}$ with a FWHM of about 2.7 \AA , covering from 3400 \AA to 4750 \AA . The optical system was designed to tolerate some vignetting at the edges of the FoV of the detector. The effect of this vignetting decreases gradually the efficiency at the corners of the CCD involving 30% of the fibres

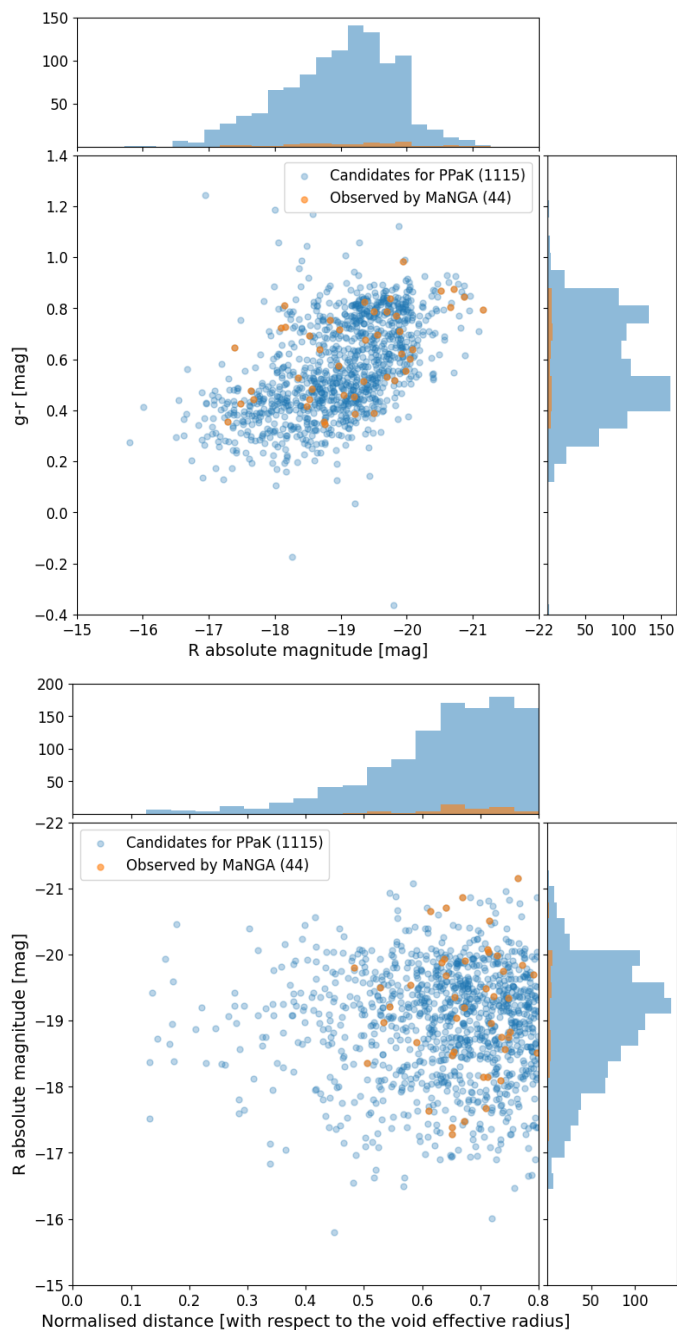


Fig. 2. Top panel: Colour-magnitude diagram of the CAVITY 1115 observable galaxies. Bottom panel: Distribution of the projected distance of the 1115 observable galaxies to the centre of the void normalised to the R_{eff} of the void with respect to the R-band absolute magnitude. In both panels the 44 MaNGA galaxies included in the parent sample have been indicated in orange.

(15% of the fibres for the most severe cases) and therefore the wavelength coverage is reduced up to a $\sim 25\%$. The vignetting presents a ring-like structure around the centre of the FoV (see Fig. 11 of Husemann et al. 2013). The useful wavelength range varies in those fibres affected by vignetting, being in the worst cases reduced to 4240-7140 Å and 3650-4650 Å for the V500 and V1200, respectively.

Similarly to the observations carried out for the CALIFA survey, we follow a three-position dithering pattern in order to have a 100% filling factor on the aperture (given the parallelism be-

tween CALIFA and CAVITY observing strategies, we encourage the reader to check Sánchez et al. 2012, for a complete summary of technical details regarding PMAS data). Exposure times for the V500 vary between 1.5 and 3.0 hours of total integration, depending on the brightness of the galaxy. For each dithering position, two exposures of 900s are taken for the brightest targets, while for the faintest galaxies four 900s exposures are observed. For the 1.5 hour observations, one set of calibration files are taken for galaxy. For longer total integration time, two sets of calibration exposures are obtained. All observations are gathered at airmasses below 1.4.

The CAVITY pipeline follows the basic reduction procedures and steps of the CALIFA survey (Sánchez et al. 2016a). With a new architecture and improvements in efficiency, it fits the particularities of the CAVITY survey. It runs in Python 3 and uses Cython code (Behnel et al. 2011) for some specific time-consuming tasks. The reduction process includes the propagation of the Poisson plus read-out noise, cosmic rays, bad CCD columns, and the effect of vignetting. First, the four different FITS files of the $4k \times 4k$ E2V detector are combined into a single frame for each exposure. Each frame is cleaned of bad pixels, including cosmic rays using PyCosmic (Husemann et al. 2012). Then, the locations of the spectra on the CCD are measured on the continuum lamp and the small instrument flexure offsets are corrected for (≤ 0.5 pixel). Straylight contribution is measured using the few gaps between fibre traces and a 2D straylight map is subtracted to all calibration and science frames. After the extraction of all spectra using the traces and the measured FWHM of each fibre, the wavelength calibration solution is obtained from the HeHgCd arc-lamp exposures, taking into account the previous estimated offsets. The spectra are resampled to a linear grid and homogenised to a common spectral resolution. The wavelength sampling is 6 Å for the V500 and 0.7 Å for the V1200, while the spectral resolution (FWHM) over the entire wavelength range is 6 Å and 2.3 Å, respectively. Fibre-to-fibre transmission differences are corrected with sky exposures taken during the twilight. Flux calibration is applied using the master sensitivity curve derived from the observation of standard stars in several photometric nights. The atmospheric extinction along wavelength (Sánchez et al. 2007) is corrected taking into account the information of the monitored V band extinction by the Calar Alto Visual EXtinction monitor (CAVEX). The sky subtraction is performed using the 36 sky fibres distributed around the FoV. The 36 spectra, taken at the same time as the science fibres, are combined, removing outliers using a sigma-clipping rejection algorithm. The average sky spectrum is then subtracted to the science frames. The final step consists in spatially re-arranging the spectra to create a datacube. The individual frames at each dithering pointing are combined into a single frame and a flux-conserving inverse-distance weighting scheme (Sánchez et al. 2012) is used to reconstruct a spatial image of the final 993 science fibres. The cube is resampled to a pixel scale of $1''/\text{pixel}$. After the cube reconstruction, the effect of differential atmospheric refraction (DAR) is corrected by measuring at each wavelength the spatial position of the centroid of the galaxy. Finally, the datacube is corrected for Galactic extinction. In next versions of the pipeline we foresee an absolute flux calibration anchored to SDSS DR16 (Ahumada et al. 2020).

5. Data quality

In order to ensure that the data comply with the standard requirements for their use by the scientific community, we perform a

quality assessment for the data. This is done in a two-step process. First, during the data reduction, the pipeline performs a set of automatic tests on the individual spectra coming from the fibres that are run to identify possible issues with the data reduction. In a later stage, a visual inspection and preliminary analysis of each final reduced datacube are performed by at least two different members of the team to estimate the quality of the data and identify any additional problem with the reduction. In this section we briefly describe both steps, including a description of the quality estimators developed for the final stages of the data reduction pipeline. A thorough assessment of the quality of the data will be presented along with the DR1.

5.1. Tests on individual spectra

As an integral component of the data reduction process, the pipeline integrates a comprehensive array of automated tests, both at the row-stacked spectra (RSS) and cube level, that are systematically executed and documented. These tests culminate in the creation of tables and figures, which are subsequently compiled into dedicated web-based reports for each night of observation. These serve as valuable tools to assess the data quality and detect potential issues arising from the reduction process.

In order to verify the accuracy of the wavelength calibration, the nominal and recovered wavelengths of well-known night-sky emission lines in each spectrum are compared before the sky subtraction step. To estimate the central wavelength of these lines, a Gaussian function is fitted to each one, resulting in 331 estimations of the relative offsets between the nominal and recovered wavelengths. The median value derived from this is approximately 0.1 Å.

The spectral resolution of a dataset is influenced by various factors, including internal focus issues, tracing/extraction errors, and wavelength calibration inaccuracies. To estimate the actual spectral resolution for each science frame, we fit the strongest night-sky emission lines using a Gaussian function before subtracting the night-sky spectrum. The FWHM values of these lines provide reliable estimates of the final resolution at their respective wavelengths. The empirical resolution for the V500 derived from night-sky lines is ~ 6.5 Å. This corresponds to a velocity resolution of $\sigma \sim 150$ km/s.

To assess instrumental dispersion, arc-lamp frames can be used instead of science frames. However, the arc-lamp exposures are shorter and not affected by resolution degradation caused by spectral drift. The derived instrumental dispersions from arc-lamp frames are smaller and more precise. Nevertheless, the final resolution achieved in the data is closer to that estimated from night-sky lines than from arc lamps.

The galaxies in CAVITY are chosen to fit within the FoV of the central bundle of fibres, ensuring that most of the 36 sky fibres remain uncontaminated by galaxy light. The subtraction process is relatively straightforward, involving the measurement of flux from prominent night-sky lines before and after subtracting the estimated night-sky spectrum.

5.2. Inspection of datacubes

The quality control of the datacubes is carried out based on a series of graphics that are automatically generated for each galaxy after one round of observations is reduced. These graphics include: i) a white image (integrated light from 4500 to 7000 Å) of the galaxy together with a map showing its negative intensity values; ii) the spectrum of the centre of the galaxy; iii) a

two-dimensional map together with an histogram of the continuum signal-to-noise ratio (SNR); iv) maps showing two different binning schemes common in stellar population studies (Voronoi tessellation presented in [Cappellari & Copin 2003](#), and a typical elliptical binning) together with the radial profile of the SNR in the case of the Voronoi bins; v) SNR maps and histograms for the H α and H β emission lines.

All these plots facilitate the execution of the quality control and help to highlight problems with the instrument or those resulting from the data reduction, as well as identify low SNR data, targets that are unsuitable for analysis, or pointings observed under non-optimal observing conditions (affecting the cube reconstruction and then to be repeated). The inclusion of the Voronoi binning map gives an idea of the suitability of each galaxy to perform spatially-resolved studies of stellar population properties and stellar kinematics. In addition, the datacubes themselves are inspected to evaluate the presence of any evident problem that might affect the shape of the spectra.

In order to inform of the outcome of the data quality assessment, each reviewer has to fill a report for each galaxy summarising the results of the evaluation. We defined four flags that identify the most problematic and/or common issues, namely: i) CUBE: if the overall reconstruction of the cube is wrong; ii) SPECTRUM: if they present any distortion or odd feature; iii) SPATIAL_BINNING_CENTRE: if the centre used in the adopted binning schemes, chosen as the bright spaxel in the cube, is incorrect; and iv) VORONOI: if the number of resulting Voronoi bins is low, or the sizes are very large to properly study the spatially-resolved properties of the stellar populations. Besides, any other spotted issue not covered by these flags can be reported as additional comments.

The most common issues reported so far during the IFS quality control are for instance the presence of several dead fibres in the North-West part of the FoV, a wrong sky emission subtraction resulting in a North-South gradient, or the presence of some sky lines residuals in the spectra not properly flagged as bad pixels in the datacube. None of these issues are irreversible and some procedures can be applied to correct these effects (this will further discussed in DR1 paper).

5.3. Propagated noise assessment

An important part of the data reduction strategy described in Sect. 4 involves the propagation of spectroscopic errors in the datacubes. In order to assess the quality of this complex and essential step, and following [Husemann et al. \(2013\)](#), we thoroughly compare the propagated errors of the datacubes with the residuals from full spectral fitting techniques assuming that such residuals are mainly linked to noise. In particular, we make use of the combination of well-tested codes such as pPXF and GANDALF ([Cappellari & Emsellem 2004](#); [Sarzi et al. 2006](#); [Falcón-Barroso et al. 2006](#)), extensively used in the characterisation of the properties and kinematics of stellar populations in galaxies (e.g. [Sánchez-Blázquez et al. 2014](#); [Ruiz-Lara et al. 2016, 2018a](#); [Falcón-Barroso et al. 2019](#); [del Moral-Castro et al. 2019, 2020](#)). This combination of codes allows for the simultaneous fit of the spectrum stellar features via a combination of the stellar models (see [Cappellari & Emsellem 2004](#)) as well as gaseous emission lines through independent Gaussian templates (see [Sarzi et al. 2006](#); [Falcón-Barroso et al. 2006](#)). In this analy-

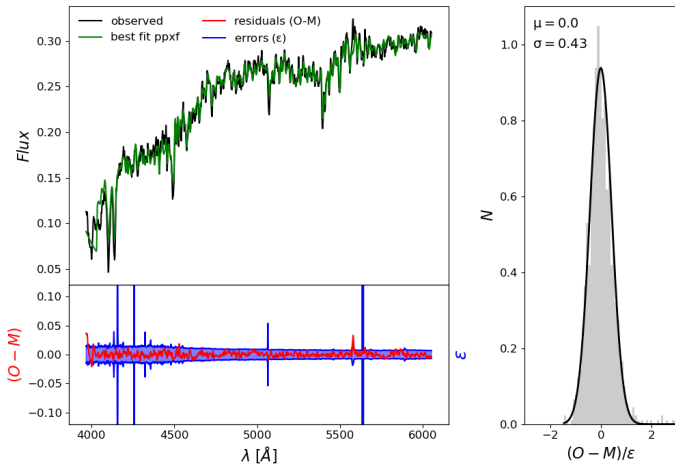


Fig. 3. Example of full spectral fitting applied to the central Voronoi bin of CAVITY 40288. In the top-left panel we overplot to the observed spectrum (black) the best fit from pPXF (green). The residuals of the fit (red) are compared to the propagated errors for the corresponding spectrum (blue) in the bottom-left panel. The right-hand panel shows a histogram of the ratio of the fitting residuals and the propagated errors including a Gaussian fit for this particular galaxy.

sis we make use of the MILES³ models constructed following the BaSTI (Pietrinferni et al. 2004) isochrones (see Vazdekis et al. 2015, 2016). This approach allows us to maximize the wavelength range covered by this analysis (including not only continuum and stellar absorption features, but also regions affected by gaseous emission).

The spectra under analysis come from applying a Voronoi binning scheme (Cappellari & Copin 2003) to the CAVITY datacubes, requesting a target SNR of 30. An example of this full spectral fitting approach applied to a typical spectrum from this spatial binning can be seen in Fig. 3. The distribution of the ratio between the residuals ($O-M$, Observed-Model, in red) and the propagated errors (ϵ) is centred at zero, with a dispersion of ~ 0.4 (slightly overestimated in this case). Fig. 4 summarises the global behaviour of all first 75 galaxies observed as part of the CAVITY project by stacking all analysed spectra. We confirm the validity of the data reduction error propagation, showing that the overall distribution of $(O-M)/\epsilon$ displays a mean value of -0.01 and a dispersion close to 1 (as expected). The run of the mean of the $(O-M)/\epsilon$ as a function of wavelength reflects that there are no clear systematic effects, although slightly larger deviations from the mean are found as we move to longer wavelengths (bottom-left panel).

6. CAVITY+: project extension

CAVITY was originally conceived as an IFS survey sampling galaxies inhabiting voids. However, with the goal of maximising the impact of the project, and mainly to fully address the proposed scientific goals, CAVITY has been expanded to include HI, CO and deep optical imaging of the IFS targets.

In what follows, we explain the main generalities of the observations and reduction of each of the sub-projects. A complete description of all these complementary observational campaigns

comprising CAVITY+ will be provided in future dedicated articles.

6.1. Single dish CO

A single dish CO spectroscopic survey was carried out on a sample of 106 CAVITY galaxies. This sample was selected from the galaxies with already available IFS data at the moment of submitting the proposal, with stellar masses above $10^9 M_\odot$ (to avoid low-metallicity objects for which the Galactic CO-to-molecular gas mass conversion factor might not apply), and excluding quiescent systems (to ensure a moderately active star formation).

For the observations, we use the 30-m telescope of the Institut de Radioastronomie Millimétrique (IRAM) at Pico Veleta (Spain) to observe $^{12}\text{CO}(1-0)$ and $^{12}\text{CO}(2-1)$ line emission. The observations were carried out between December 2021 and February 2023. We used the E090 and the E230 EMIR bands simultaneously in combination with the autocorrelator FTS at a frequency resolution of 0.195 MHz (corresponding to a velocity resolution of $\sim 0.5 \text{ km s}^{-1}$ at CO(1-0) at the frequency of our observations) and with the autocorrelator WILMA with a frequency resolution of 2 MHz (corresponding to a velocity resolution of $\sim 5 \text{ km s}^{-1}$ at CO(1-0)). The angular resolution was $\sim 22''$ and $\sim 11''$ for CO(1-0) and for CO(2-1), respectively. Each object was observed until it was detected with a SNR of at least 5 or until a root-mean-square noise (rms) of $\sim 1.5 \text{ mK}$ (T_{mB}) was achieved for the CO(1-0) line at a velocity resolution of 20 km s^{-1} . The on-source integration times per object ranged between 30 minutes and 4 hours.

The data reduction was done with the CLASS program of the GILDAS software package⁴, and involved the selection of good data, the subtraction of (linear) baselines from individual integration and the averaging of the total spectra. Some observations taken with the FTS backend were affected by platforming which was corrected using the *FtsPlatformingCorrection5.class* procedure provided by IRAM.

After generating the final CO(1-0) and CO(2-1) emission spectra, we conducted a quality control analysis. This analysis involved inspecting each CO spectral profile and searching for possible errors and inconsistencies in the data reduction process. In particular, we checked the following points. (i) We visually inspected the spectra to make sure that the detections are convincing with no indications of artefacts. (ii) We confirmed that the baselines are flat, as wavy baselines can indicate an incorrect baseline subtraction or contamination with poor-quality data. (iii) We checked that the defined velocity window accurately constrained the entire CO emission and was centered on the recession velocity derived from the optical redshift. (iv) We confirmed the consistency between the CO(1-0) and CO(2-1) lines: the CO(1-0) line width is expected to be similar or larger than the CO(2-1) line width, which is due to the smaller beam at the higher frequency of CO(2-1) emitted from a smaller area.

To perform this analysis, we produced plots of the CO(1-0) and CO(2-1) lines at various velocity resolutions (10, 20, and 40 km s^{-1}) to gain a different perspective of the data, which allowed us a more thorough inspection of the spectra. As mentioned before, one of the requirements was to observe each object until it was detected with a SNR of at least 5 or until a rms of $\sim 1.5 \text{ mK}$ (T_{mB}) was achieved for the CO(1-0) line at a velocity resolution of 20 km s^{-1} . A priori this requirement ensured high quality for the CO data in general.

³ The models are publicly available at <http://miles.iac.es> and are based on the MILES empirical library (Sánchez-Blázquez et al. 2006; Falcón-Barroso et al. 2011).

⁴ <http://www.iram.fr/IRAMFR/GILDAS>

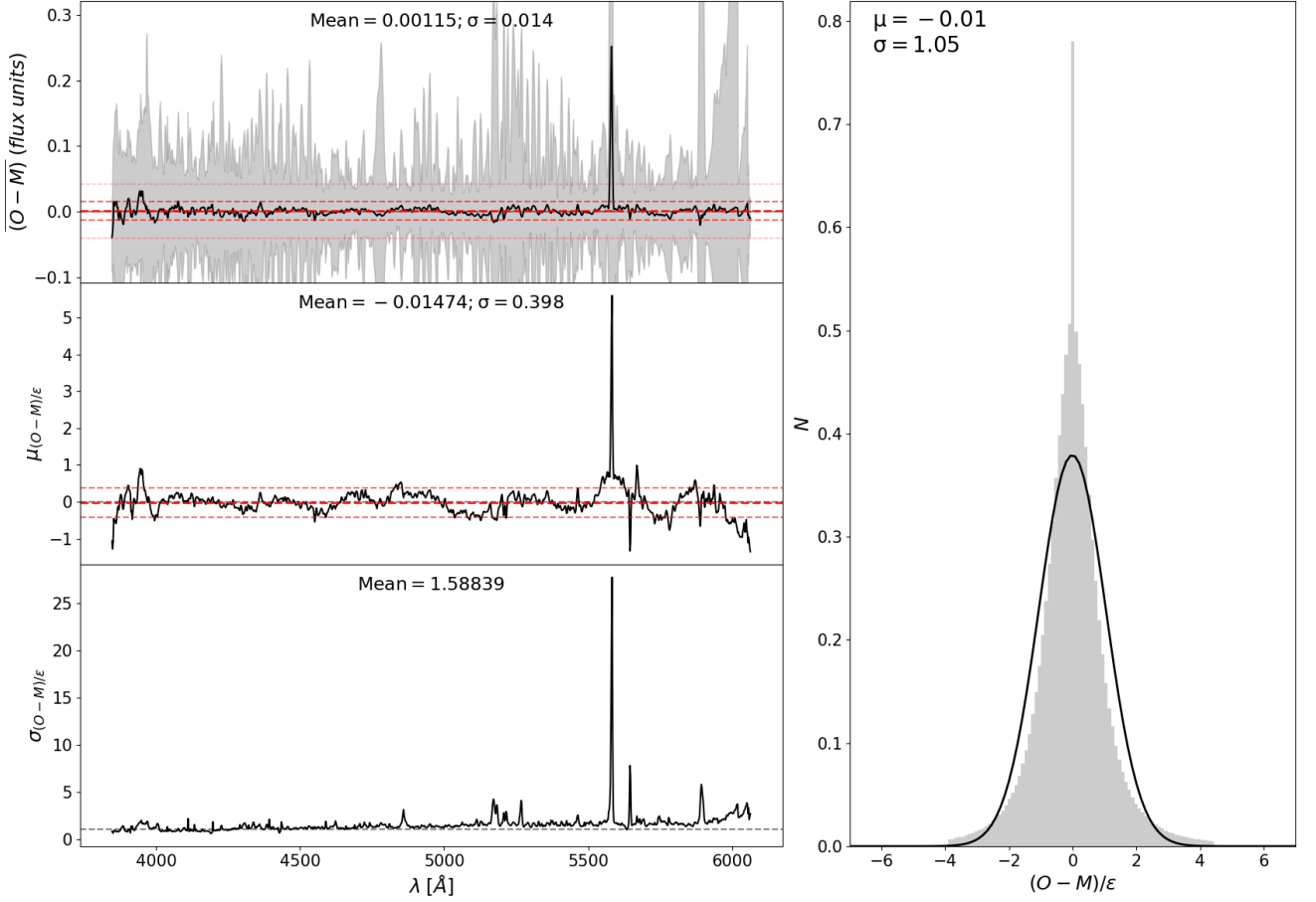


Fig. 4. Comparison between the full spectrum fitting residuals and propagated errors in the CAVITY datacubes using a Voronoi spatial binning scheme. Top-left panel: residual spectrum averaged over all Voronoi bins and all the CAVITY galaxies analysed. Middle-left: Mean of the ratio between the residuals and the propagated errors $((O - M)/\epsilon)$ as a function of wavelength. Bottom-left: Dispersion of $(O - M)/\epsilon$ as a function of wavelength. Right hand panel: Global distribution of the $(O - M)/\epsilon$. Red horizontal lines of gradual thickness are plotted in each panel for the mean value, mean $\pm \sigma$, and mean $\pm 3\sigma$. A Gaussian distribution representative of the mean and dispersion of the $(O - M)/\epsilon$ distribution is represented in the right-hand panel. In this analysis regions flagged as bad by the reduction pipeline have been masked from each individual spectrum as well as the 5577Å sky line.

Further details about the observations, sample selection, data reduction and the presentation of CO data will be published in Rodríguez et al. (2024, in prep).

The CO-CAVITY will be crucial to evaluate the gas reservoirs for future star formation in void galaxies. We will be able to compare the molecular gas mass to the SFR, the stellar mass, and the atomic mass (see Sec. 6.3) in order to search for possible trends in the star formation processes in different large-scale environments.

6.2. Interferometric CO

Interferometric CO(1-0) data have been secured from the Atacama Large Millimeter/submillimeter Array (ALMA) for a subsample of 41 galaxies at similar resolution than the IFS data (less than 1 kpc). The first observations happened in a Cycle 9 program and are ongoing with highest priority in a Cycle 10 program to complete the requested observations with over 40 hours.

For the observations we use the 12-m array in three different configurations (C1, C3, and C4) corresponding to baselines from 0.16 to 0.78 km. We observe the low frequency CO(1-0) line (115 GHz) at a frequency resolution of 1.13 MHz (corresponding to a velocity resolution of $\sim 3 \text{ km s}^{-1}$). The achieved angular

resolutions of 1-1.5'' ensure linear resolutions better than 1 kpc ($\sim 350 \text{ pc/arcsec}$ at 4800 km s^{-1} and $\sim 900 \text{ pc/arcsec}$ at 10600 km s^{-1}). The average SNR for a typical 1 arcsec^2 portion in any of the galaxies is 4.5 in the lower 25% distribution, 10 in the lower 50% distribution, and 20 in the lower 75%. The on-source integration time per object is around 30-50 min.

The data reduction is done with the ALMA pipeline (CASA, <https://casa.nrao.edu/>) and quality assurance following the standards of the observatory. Further details about the observations, sample selection, data reduction and the presentation of ALMA data will be published elsewhere.

This is the first interferometric CO survey of a statistically significant sample of void galaxies, which together with CAVITY IFS data, will allow us to elucidate the spatially-resolved molecular gas properties and potential variations of SFE in this largely unexplored type of galaxies.

6.3. Atomic gas (HI)

Together with CO, HI data is key in order to have the full information of the neutral gas content necessary to understand the matter assembly and how the process of SF occurs in these galaxies. Thus, a dedicated observing campaign of 146 hours has

been executed with the Green Bank Telescope (GBT) to observe 78 CAVITY galaxies with CO information from IRAM 30m (see Sec. 6.1) and for which no HI spectra was available from the literature (the ancillary data –coming mostly from the ALFALFA project at Arecibo 305m– will allow us to characterise the HI in the full CO-CAVITY sample). We use the L band, with a bandwidth of 11.72 MHz. To observe the rest frequency of the HI line (1.420 GHz) the (sky) topocentric frequencies for the different sources are in between 1.378 – 1.355 GHz. We will obtain calibrated HI spectra with channel widths of about 20 km s⁻¹, and the HPBW of the telescope at these frequencies is $\sim 9'$. The on-source integration times per object range between 30 minutes to a few hours.

The data reduction is done with GBTIDL (<https://gbtidl.nrao.edu/>). Additional details about the observations, data reduction and the presentation of HI data will be published elsewhere.

These observations will allow us to characterise the HI mass of the galaxies and measure HI profile asymmetries, and relate them with internal properties such as the stellar component, bars and morphological type, as well as external properties related to their galactic environment.

6.4. Deep optical imaging

We are currently carrying out an extensive observational campaign with the 2.54-m Isaac Newton Telescope (INT) in order to provide deep imaging of the CAVITY galaxies. We use the Wide Field Camera (WFC), located at the primary focus, with a 4 CCD detector covering a FoV of approximately $34' \times 34'$ with a pixel scale of $0.333''$. We use the SDSS g and r filters.

Observations have been allocated since semester 21A onward from both the NL-PC and CAT time allocation committees. To date, we have observed a total of 127 fields containing 141 CAVITY galaxies with IFS observations. In addition, a careful examination of the fields, to make the most out of each observing night, arose a total of 277 void galaxies (within the 15 voids that are targeted within the CAVITY project) with deep imaging in g and r bands reaching down to 30+ mag arcsec⁻². All observations were carried out mainly in dark time, with some cases of grey time. Exposure times are nominally 1.5h per band, which can be increased if more exposure time is needed to reach the desired depths in case of moonlight.

The observational campaigns are designed with the aim of producing highly efficient flat-fielding at low surface brightness. For this purpose strong dithering patterns have been carried out that allow the science images themselves to be used to produce the flat image, a process that we detail below. The reduction is performed in what we call a “run”. This run consists of a set of images, typically the set of nights observed over a period of a few weeks, in which we assume that the flat-fielding has no variation, so therefore can be corrected by a single flat image obtained from this run. For each night, the images are bias subtracted with a standard procedure. Subsequently, the bias subtracted images are heavily masked using SExtractor (Bertin & Arnouts 1996a) and NoiseChisel (Akhlaghi & Ichikawa 2015), normalised, and combined, producing a flat image. This flat is applied to the images producing the final reduced images.

For the combination of each of the observed fields, we make a provisional astrometric solution with the *astrometry.net* package (Lang et al. 2010), which is then refined with SCAMP (Bertin 2006). The co-adding process consists of a routine in which, through iterations of masking and sky subtraction, we converge to a final solution that we consider the final co-add.

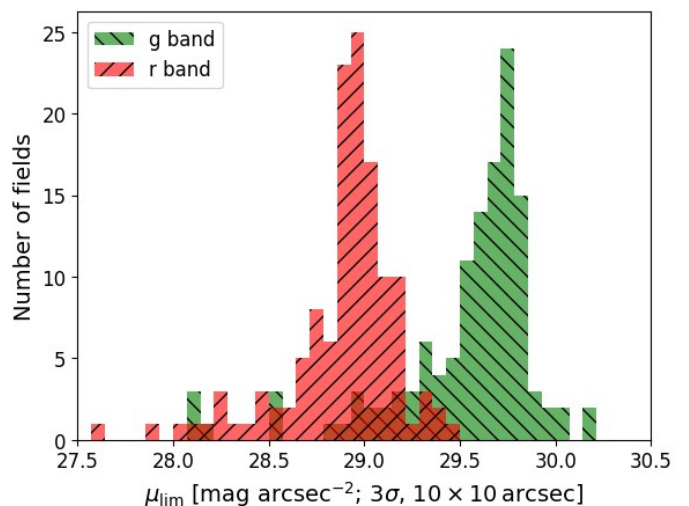


Fig. 5. Histogram of surface brightness limits in optical g and r bands measured at 3σ , in 10×10 arcsec boxes for the INT data (for details on the procedure see Román et al. 2020).

This methodology is considered the most robust for producing highly efficient images in the low surface brightness regime (Watkins et al. 2024). First we produce a seed co-add, which will be the beginning of the iteration. This co-add is produced by a constant sky subtraction for the whole image. This ensures that no over-subtraction of the data occurs in this seed co-add, however there are certain gradients that are targeted to be removed by the process. To do this, after producing a mask in this co-add, this mask is applied to the individual exposures. We perform a sky subtraction on these individual exposures using Zernike polynomials (Zernike 1934). The motivation for using Zernike polynomials is to produce a sky subtraction compatible with the gradients of an optical system, minimising the potential over-subtraction of real sources present in the images (see e.g., Zhang et al. 2023; Román et al. 2023). The images are then photometrically calibrated using SDSS and the noise of each individual image is calculated. The images are then combined by a 3σ resistant mean, this mean being weighted by the individual noise of each image, producing the co-add that will be used as a new seed in this iterative process. This process of masking, sky subtraction and combination to obtain the co-add is repeated a number of times until a final co-add with excellent sky subtraction is achieved. We find that 3 iterations using low order Zernike polynomials, typically order 3, is sufficient. However, images with the presence of the moon or at low altitude require more iterations and a Zernike polynomial order of 4. Fig. 5 presents histograms of surface brightness limits in the r- and g-bands. The depth analysis shows distributions in the g and r bands with peaks of approximately 29.7 mag arcsec⁻² in the g band and 29.0 mag arcsec⁻² in the r band, measured using a 3σ in 10×10 arcsec boxes metric (see Román et al. 2020). We can notice tails in the distributions with shallower images, for instance below 29.5 mag arcsec⁻² in g – band and 28.7 mag arcsec⁻² in r – band. These are exclusively due to the presence of the moon in the observations. As far as possible, future observations will add additional exposure times to these shallower images, in order to have homogeneity in the depths reached, avoiding images with shallower data. In the case of the computation of surface brightness profiles, this translates to even fainter magnitudes (see Sect. 7.2).

To ensure the high quality of the deep imaging data, we carry out a visual inspection of the data when a set of new observa-

tions is processed by the deep imaging reduction pipeline. The revision is performed on each observed band per galaxy, with the redundancy of the pixels of each image. Because of the size of WFC/INT FoV, the full image covers an area much larger than the CAVITY galaxy size. This allows us to look for any possible source of contamination by close galaxies, stars, or cirrus from the Milky Way. We therefore perform a visual inspection on the full images and a zoom area on the CAVITY galaxies. We defined a list of flags to identify any characteristic that could be related to an issue during observations, a problem derived from the reduction pipeline, or any characteristic that could be relevant when working with the data. We defined the following flags for the full images: i) STRIPES: if vertical or horizontal stripes, positive or negative ghost light, or artefacts are presented in the images; ii) INHOMOGENEOUS: if the images present irregular or not uniform background and fluctuations; iii) SPIKES: if there are stellar spikes, or bright spikes by other sources; iv) EXTERNAL_OBJ: if there is any external object in the images (e.g., satellites, asteroids); v) REFLECTIONS: if there is any residual light affecting the full image; vi) DITHERING: if there is any issue with the dithering, like a pattern or lack of some pointings in the observations. When focusing on a CAVITY galaxy, we noted if the previous characteristics were affecting the galaxy as well, in addition to the following flags: i) STAR_HALOS: if the galaxy image is affected by the stellar halo light from a close bright star; ii) STAR_PUNCTUAL: if the galaxy image is affected by the light coming from a bright punctual star; iii) GALAXY_HALOS: if the galaxy image is affected by the halo light from a close bright galaxy; iv) LSB_FEATURES: if there are distinguishable low surface brightness (LSB) features such as interactions, streams, shells, or tails. In addition, we provide comments to report any extra characteristic or issue not covered by the flags (for instance serendipitous events).

After the first round of the deep imaging quality control, we find that around 30% of the fields are affected by stripes inhomogeneities, and spikes, that are quantified and taken into account in the analysis of the data, these are the typical artefacts found in this type of data-sets and do not impair the science analysis in most of the cases. In general, the field images are not much affected by external objects or reflections, and only in a few cases there is a problem related to dithering. When present, the reports were considered in each subsequent observation and reduction process. For the CAVITY galaxies, about 30% of the images are affected by light coming from a bright nearby star, while 20% are affected by a nearby bright galaxy.

The deep-imaging CAVITY follow-up will allow us to detect low-surface brightness (LSB) structures indicating possible interactions, low-mass companions, or other local environment indicators that can help us to characterise their influence in the evolution of void galaxies. In the first round of observations, we detected LSB features in 26% of the CAVITY galaxies. An example of LSB features found in a few CAVITY galaxies is shown in Fig. 6. For a more in-depth assessment of the science to be done with these data, in Sect. 7.2 we present some examples of surface brightness profile determination.

7. CAVITY science

The IFS database for the 300 galaxies of the CAVITY survey, together with all additional information coming from the CAVITY+ extended project, will offer a unique opportunity to explore the properties of galaxies residing in cosmic voids and will allow to address a large number of astrophysical questions.

Within the expertise of the CAVITY team there is an interest to explore the following aspects of galaxies in voids:

- Baryonic mass assembly
- Impact of the large-scale environment on the gas accretion
- sSFR and the molecular and atomic gas content of void galaxies
- Merger and accretion histories of galaxies from the light distribution in the outer parts of galaxies
- Influence of the local- vs the large-scale environment on general galaxy properties
- Effects of the large-scale structure in the prevalence of AGNs, their properties, and their role in quenching/enhance star formation in void galaxies
- Properties and formation of dwarf galaxies in voids

We have already carried out some preparatory analysis of the SDSS spectroscopic data of the central parts of the galaxies within the CAVITY parent sample (Domínguez-Gómez et al. 2023a,b) where we concluded that the stellar mass assembly of void galaxies occurs slower than in filaments and walls, and much slower than in clusters, pointing to different physical drivers of the galaxy evolution for the different large-scale environments. Furthermore, the analysis of the stellar mass-metallicity relation on the same sample shows that the enrichment also occurs differently in the different large-scale environments. These works, although ground-breaking, lack the 2D information crucial to discern among the different physical processes that drive the different SFHs at different densities.

In this section, as an example of the power of combining CAVITY and CAVITY+ data and to present the type of products that will be produced by the collaboration, we have selected a sample of four CAVITY galaxies that will serve as pilot sample for the CAVITY science. These galaxies are CAVITY10668, CAVITY48125, CAVITY49137, and CAVITY59902 (see Table 1). For all galaxies we have IFS, INT deep imaging, and single-dish CO data, except for CAVITY49137, a barred galaxy in a triple system with only IFS data available so far. The selected galaxies show similar absolute magnitudes in *r* band (ranging from -19.53 to -20.37 mag) and a wide range of *g* – *r* colours (from 0.549 to 0.852 mag). The purpose here is to show the power of the CAVITY data to gather kinematic, chemical, and physical properties of their gas and stars to be linked to local interactions, global environmental effects, and secular evolution. The characterisation of these properties on the full CAVITY sample will enable addressing the main science drivers of the project. For this purpose, we analyse and present here the data products from the IFS, the deep imaging, and the CO survey for these four galaxies.

7.1. Gas and stellar population properties

To analyse the CAVITY datacubes presented in this work, we have used Pipe3D (Sánchez et al. 2016c,b), which was developed to characterise the stellar and ionised gas properties as derived from optical spectra, in particular, it has been optimised to work with optical IFS data. Specifically, we have made use of pyPipe3D, the new publicly available implementation for Python (Lacerda et al. 2022).

In order to derive 2D maps of the stellar properties, pyPipe3D first performs a spatial binning called Continuum Segmentation binning (CS-binning) to increase the SNR of the spectra and obtain an accurate estimation of the stellar contribution. This binning scheme combines a continuity criterion for the surface brightness (applying a specified maximum difference in

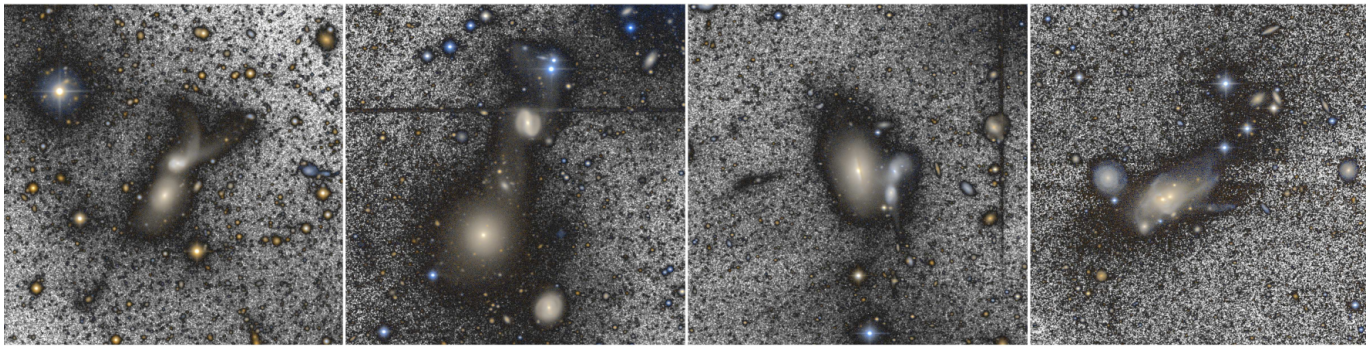


Fig. 6. Composed image for a sample of CAVITY galaxies with undetectable tidal tails in shallower data, but detected in the CAVITY INT deep images, with $\mu_g \sim 28 \text{ mag arcsec}^{-2}$ in the g-band. The colour image is constructed with the g and r bands. The dark background with the sum image g + r in high contrast.

the flux intensity to aggregate adjacent spaxels) and a goal for the SNR ratio (in our case, 50). Then, the code fits each spectrum by a linear combination of single stellar population synthesis model (SSP) spectra after correcting for the appropriate systemic velocity and velocity dispersion and taking into account the effects of dust attenuation (Cardelli et al. 1989, with $R_V = 3.1$). As SSP templates we use the MILES (Vazdekis et al. 2015) stellar synthesis models (BASE models) using the BaSTI isochrones (Pietrinferni et al. 2004). We use the Kroupa Universal Initial Mass Function (IMF, Kroupa 2001), with an IMF slope of 1.3.

Once we have an estimation of the stellar continuum, pyPipe3D performs a procedure called *dezonification* to decouple the analysis of the emission lines from the spatial binning required for the stellar populations, taking into account the relative contribution of each spaxel to the spatial bin in which it is aggregated (Cid Fernandes et al. 2013). The *dezonification* map is multiplied to the stellar model of the datacube and the resulting cube is spatially smoothed with a Gaussian kernel to obtain a continuous model of the underlying stellar population. Finally, this model is subtracted from the original datacube providing a pure emission line cube. For the analysis of the emission lines, the algorithm performs a multi-component fitting on the pure gas cubes using a single Gaussian function per emission line plus a low-order polynomial function. The treatment of the errors is done via a Monte Carlo simulation, and it includes the propagation of the uncertainties from the subtraction of the underlying stellar population to the parameters derived for the emission lines. A full description of the whole procedure performed by Pipe3D can be found in Lacerda et al. (2022) and Sánchez et al. (2016b). Figure 7 illustrates the quality of the performance of pyPipe3D showing as an example the fit of the central spectrum (5'' diameter) of CAVITY49137.

Figure 8 shows typical data products of the IFS cubes for the selected sample of four void galaxies applying the above explained methodology. The ionised gas abundance maps have been derived from the pyPipe3D emission line intensity maps using the O3N2 strong-line abundance indicator with the Marino et al. (2013) calibrator. The light-weighted $[Z/H]$ maps have been directly obtained from pyPipe3D as described in (Lacerda et al. 2022, see Eq. 12). For the objects that also have deep imaging and CO data available, the CO(2-1) and CO(1-0) spectroscopic profiles as well as the optical deep images and surface brightness profiles are shown in Figs. 9 and 10.

Figure 11 shows a quick quality assessment of the IFS datacubes included here, we present SNR maps (and histograms) of the galaxies with contours indicating a SNR level of 10 and 30, respectively. According to experience, this would correspond

to the area within the galaxy for which we can provide reliable kinematics and stellar parameters. The quality of the CAVITY datacubes will enable gathering spectroscopic information reaching a surface brightness of around $23 \text{ mag arcsec}^{-2}$ with a $\text{SNR} \sim 30$, and down to nearly $25 \text{ mag arcsec}^{-2}$ with a $\text{SNR} \sim 10$.

Table 2 shows some average properties derived from the previous analysis. Among other quantities, the average stellar ages and metallicities at one effective radius (R_{eff}), as well as the ionised gas averaged metallicity at the same radius are shown. The average stellar metallicities and ages are in agreement with the $MZ_{\star}R$ (stellar mass-metallicity relation) for void galaxies with long-time SFHs, defined as those galaxies that formed a low fraction of their stellar mass ($< 21.4\%$) 12.5 Gyr ago, but formed stars uniformly over time (Domínguez-Gómez et al. 2023a).

According to the criteria of local environment defined in Argudo-Fernández et al. (2015) two of the galaxies are in isolation, CAVITY48125, and CAVITY59902; whereas CAVITY10668 is part of an isolated pair and CAVITY49137 lives in a widely separated triple system. The two isolated systems, as expected, show symmetric kinematic, stellar age, and metallicity maps. In particular, we see a clear alignment between gas and stellar kinematics, an aspect that we do not see in CAVITY10668 (especially) or CAVITY49137, where some differences can be seen between the stellar and gaseous kinematics. INT imaging of these two isolated systems display quite symmetric discs up to the outermost regions, though some subtle asymmetries are detected by our deep imaging in their outskirts.

CAVITY10668 is an interacting pair and the velocity maps show a clear misalignment between the ionised gas and the stellar distribution, as well as asymmetries in the age and metallicity distributions. The ionised-gas distribution is aligned with the elongated light distribution of the galaxy itself, whereas the stellar kinematics is more oriented towards its companion⁵. The ionised-gas metallicity map shows an increase in metallicity towards the tail with the interacting galaxy (to the north of the image). The stellar metallicity shows a lowering of the metallicity towards the central regions and an increment towards the North-West of the image, towards the location where the companion is placed. The CO spectra for this galaxy is centrally concentrated at zero velocity, possibly linked to a concentration of molecular gas in the central regions. This interpretation would be compatible with the ionised-gas kinematic 2D map (see Figure 8) that

⁵ At this point we must say that CAVITY10669, the companion to CAVITY10668 and seen in the INT deep imaging, was also observed as part of CAVITY but with poor weather conditions. We plan to reobserve this system in order to fully study this interesting pair.

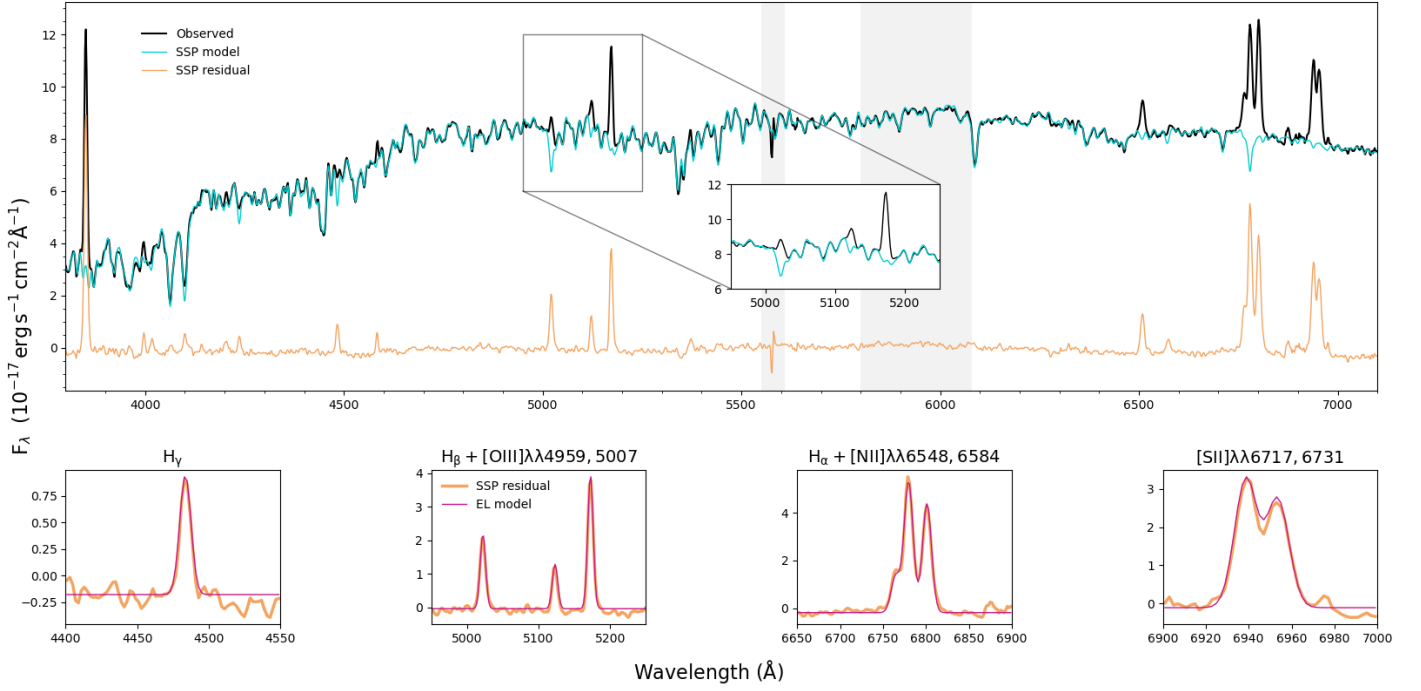


Fig. 7. Example of a pyPipe3D fit to the central spectrum (5'' diameter) of CAVITY49137 extracted from the IFS datacube. In the top panel, the black line represents the original spectrum, along with the best fitted stellar population (SSP model, cyan). The pure emission line spectrum after subtracting the best stellar population model is shown as a solid yellow line (SSP residual). The inset is focused on the $H\beta$ -[OIII] spectral region to highlight the quality of the fit. The vertical shaded regions indicate the wavelength ranges masked during the fitting process. The bottom panels show some examples of emission line fittings (emission line (EL) model, red line).

Table 1. Void galaxy properties

CAVITY ID	redshift	$g-r$ absolute magnitude [mag]	r-band [mag]	Stellar mass [$\log(M_{\odot})$]
10668	0.03773	0.640	-20.366	9.840
48125	0.03293	0.714	-20.021	10.399
49137	0.03308	0.852	-20.005	10.486
59902	0.02993	0.549	-19.529	9.909

Table 2. Void galaxy average stellar and gaseous properties

CAVITY ID	Molecular mass $\log(M_{\odot})$	$\langle \log(\text{age}[\text{yr}]) \rangle$	$[Z/H]_{\text{R}_{\text{eff}}}$	$12+\log([O/H])_{\text{R}_{\text{eff}}}$	$\sigma_{\text{R}_{\text{eff}}}$ [kms^{-1}]
10668	9.50 ± 0.04	9.0 ± 0.2	-0.3 ± 0.3	8.56 ± 0.03	150 ± 20
48125	9.32 ± 0.04	9.1 ± 0.2	-0.2 ± 0.2	8.57 ± 0.05	160 ± 20
49137	—	9.6 ± 0.2	-0.1 ± 0.2	8.47 ± 0.04	50 ± 20
59902	8.85 ± 0.06	8.8 ± 0.2	-0.3 ± 0.2	8.50 ± 0.04	120 ± 10

shows zero velocity contours only in the central regions. The kinematic misalignment, the metallicity asymmetries, and the CO concentration can all be consequence of the interaction state in which this galaxy is found. The other non-isolated system, CAVITY49137, shows also asymmetries in all the maps, no deep imaging is available for this galaxy, but a visual inspection of the DECALS image (Dey et al. 2019) shows some signs of lopsidedness in the light distribution of this barred galaxy that needs to be confirmed with deeper imaging. The twisted iso-velocity contours present in the central parts of the gas kinematics are probably due to the presence of a clear bar (e.g. Seidel et al. 2015). The CO(2-1) and CO(1-0) data are still not available for this galaxy.

The few examples presented here are proof of the capability of the CAVITY survey to characterise the spatial stellar and gas properties of galaxies inhabiting voids for the first time in a statistical sample, a first study on the spatially-resolved stellar populations of 118 CAVITY galaxies has been recently submitted for publication (Conrado et al. 2024, submitted). The combination with deep optical imaging and CO observations will allow us to determine the effect of local and global environment on the galaxy properties, providing with a unique view of galaxies in cosmic voids.

7.2. Deep imaging and light distributions

A visual inspection of the deep images we are gathering already reveals the variety of galaxies in cosmic voids (see Fig. 6). These deep images from the CAVITY+ INT campaign are clear evidence that void galaxies, contrary to the intuition, are not necessarily isolated systems. Indeed, the four galaxies selected for this presentation paper inhabit different local environments as well, highlighting this fact. Apart from allowing us to study the more local environment of the CAVITY galaxies, the deep imaging data unveil a large number of low surface-brightness structures⁶ providing a perfect complement to the IFS data and, in some cases, CO information.

In principle, one might expect that internal evolutionary effects are more important in void galaxies than environmental effects as they inhabit these low density regions of the Universe. However, the effects of minor mergers should not be neglected. As such, a thorough characterisation of the outer parts, including the study of the surface brightness profiles and asymmetries, can shed light into the past accretion histories of the analysed galaxies. The large number of galaxies that are being observed as part of this deep imaging campaign enables an unprecedented comparison between accretion histories of galaxies in different environments. This, in combination with the IFS and CO data (and other ancillary comprising CAVITY+, see Sec. 6) will complete the puzzle of how these galaxies have formed and evolved.

In the line of the previous section, here we analyse the surface brightness (SB) profiles of CAVITY10668, CAVITY48125, and CAVITY59902 (the ones with INT data so far, see Fig. 10). In the case of galaxies in interaction, such as CAVITY10668, low SB features and asymmetries abound, hindering the interpretation of their SB profiles. In the case of more isolated galaxies (like CAVITY48125 and CAVITY59902) the analysis of their outer regions is enabled. Figure 10 exemplifies our process of computing SB profiles and compare the profiles from the INT campaign to those from DECALS.

In short, we measure the surface brightness profiles of each of the galaxies in the *g*-band image. Proper local background subtraction and image masking need to be done to study the low SB regions. We construct masks for each image using the software SExtractor (Bertin & Arnouts 1996b, v.2.25.0). We combine two different masks, the first one with the parameters optimised for detecting extended sources (larger background size and intermediate threshold) and the other one optimised for point source detection (lower background size and threshold). Additionally, we mask all peaks detected in the residual mask of the image minus a Gaussian smoothed version of the image that are larger than the PSF (FWHM ~ 1.2 arcsec). Finally, we visually inspect the mask and refine any region by hand. With all the contaminant sources masked properly, we measure the local background in boxes around the galaxy. We set the distance of the boxes to be larger than the region where an elliptical profile of the galaxy is flattened. Then, we typically placed around $\sim 10 - 20$ boxes of at least 50 not-masked pixels around the galaxy and we measure the mean of all pixels not masked inside the boxes rejecting pixels above 2.5 times the standard deviation. Then, we set the local value to be the mean of all boxes. The dominant uncertainty at this level is the value of the local background, so we measure the error on this value as the standard deviation of all the boxes. We construct SB radial profiles using the implementation in astropy (Astropy Collaboration et al. 2013, 2018, v5.1) of the method described by Jedrzejewski

(1987). This method fits elliptical apertures at each radial bin. We increase the spacing between each aperture logarithmically, using 2% bigger radii than the previous aperture.

As a general remark, we can see how we reach around 1 to 2 mag arcsec⁻² deeper than with the same approach applied to DECALS data. For the cases of the isolated systems (CAVITY48125 and CAVITY59902) we can see how reliably reaching a magnitude of ~ 30 mag arcsec⁻² is a reality, starting to grasp emission from the halo of the analysed galaxies, and even a faint tidal tail as the one seen on the north side of CAVITY48125. In the case of CAVITY10668, the outermost regions are clearly affected by the presence of the companion galaxy. Interestingly, in the case of CAVITY48125 and CAVITY59902 we see clear downbending profiles (Pohlen & Trujillo 2006). However, the origin of both profiles seem to be different. Whereas in the case of CAVITY48125 the so-called *break* is located at the end of the spiral pattern, and probably linked to it (Debattista et al. 2006), for CAVITY59902 it does not seem to be clearly related to any morphological feature, and thus, probably related to its mass distribution (due to a change in the angular momentum of the disc or a star formation threshold, see e.g. Roškar et al. 2008; Sánchez-Blázquez et al. 2009). These profiles evidence the importance of relying on deep imaging data in order to properly characterise the outskirts of the galaxies, more susceptible to environmental effects (Sánchez-Alarcón et al. 2023).

8. Conclusions

The Calar Alto Void Integral-field Treasury Survey, CAVITY, aims to understand the influence of the large-scale environment on galaxy formation and evolution. For that, CAVITY is gathering new observations that are crucial to unveil the past history of the observed galaxies. To date, CAVITY is the largest and more complete survey on the detailed properties of void galaxies. The survey was initiated as an IFS survey using the PMAS/PPAK spectrograph at the 3.5 meter telescope at the Observatory of Calar Alto, Spain. This initial survey has been extended to a CO, HI, and optical deep imaging follow-up of the sample. The single dish CO(1-0) and CO(2-1) emission observations are coming from the IRAM 30m telescope, resolved CO(1-0) data are collected with ALMA, HI spectra are obtained with the Green Bank Telescope, and the deep *g*- and *r*-band imaging is being carried out at the Wide-Field-Camera at the Isaac Newton Telescope at La Palma Observatory. These complementary data-sets conform the CAVITY+ project.

We have presented here the parent sample from which the 300 galaxies that will form CAVITY have been selected. These 300 galaxies populate 15 nearby voids, sampling across the voids with around 20 galaxies per void, and populating the colour-magnitude diagram. This ensures that CAVITY will offer a complete view of the properties of galaxies in voids. A quick outline of the observations, data reductions, as well as quality of the data has been given in this presentation paper, although separate, in-depth papers are planned to fully present the CAVITY as well as the CAVITY+ data.

To give the community a feeling of the quality of the data and products that will be released in the CAVITY project, apart from the assessment carried out in Sect. 5, we have presented data-products for four galaxies. We have shown that we will provide 2D stellar ages and metallicities, as well as ionised gas properties, and stellar and gas kinematics up to the outer parts of these galaxies. We have presented results for two isolated galaxies, an interacting one and an example of a small group residing in cosmic voids (proving that some galaxies in voids present a rich lo-

⁶ All these features and structures will be thoroughly analysed in future work within the CAVITY collaboration.

cal environment). These results show that kinematic, stellar and gas properties substructures, asymmetries and gradients can be derived from the data. These spatially resolved parameters will be key to constrain the evolution of galaxies residing in cosmic voids. Deep imaging provides the extra information about possible local environment processes driving some internal properties (beyond the field of view of the IFS data) as well as SB profiles down to 30 mag/arcsec². The addition of CO, and HI data will help to evaluate the gas reservoirs and the star formation efficiency in void galaxies.

A first data release will be open to the community in July 2024, offering datacubes, for a sample of around 100 galaxies, through an easy accessible data-base platform based on the Daiquiri framework, at the survey web-page (cavity.caha.es).

Acknowledgements. Based on observations collected at the Centro Astronómico Hispano en Andalucía (CAHA) at Calar Alto, operated jointly by Junta de Andalucía and Consejo Superior de Investigaciones Científicas (IAA-CSIC). We acknowledge financial support by the research projects AYA2017-84897-P, PID2020-113689GB-I00, and PID2020-114414GB-I00, financed by MCIN/AEI/10.13039/501100011033, the project A-FQM-510-UGR20 financed from FEDER/Junta de Andalucía-Consejería de Transformación Económica, Industria, Conocimiento y Universidades/Proyecto and by the grants P20-00334 and FQM108, financed by the Junta de Andalucía (Spain). TRL acknowledges support from Juan de la Cierva fellowship (IJC2020-043742-I). LSM acknowledges support from Juan de la Cierva fellowship (IJC2019-041527-I). DE acknowledges support from a Beatriz Galindo senior fellowship (BG20/00224) from the Spanish Ministry of Science and Innovation. RGD, RGB, and AC acknowledge financial support from the State Agency for Research of the Spanish MCIU through ‘Center of Excellence Severo Ochoa’ award to the Instituto de Astrofísica de Andalucía, CEX2021-001131-S, funded by MCIN/AEI/10.13039/501100011033, and to financial support from the projects PID-2019-109067-GB-I00 and PID2022-141755NB-I00. HC also acknowledges support from the Institut Universitaire de France and from the CNES. IMC acknowledges support from ANID programme FONDECYT Postdoctorado 3230653. JF-B acknowledges support from the PID2022-140869NB-I00 grant from the Spanish Ministry of Science and Innovation. VQ, SP, and MH acknowledge that this work has been supported by the Agencia Estatal de Investigación Española (AEI; grant PID2022-138855NB-C33), by the Ministerio de Ciencia e Innovación (MCIN) within the Plan de Recuperación, Transformación y Resiliencia del Gobierno de España through the project ASFAE/2022/001, with funding from European Union NextGenerationEU (PRTR-C17.11), and by the Generalitat Valenciana (grant PROMETEO CIPROM/2022/49). PSB acknowledges financial support from the from the Spanish Ministry of Science under the projects with references: PID2019-107427GB-C31 and PID2022-138855NB-C31. PVG acknowledges that the project that gave rise to these results received the support of a fellowship from “la Caixa” Foundation (ID 100010434). The fellowship code is B005800. AFM acknowledges support from RYC2021-031099-I and PID2021-123313NA-I00 of MCIN/AEI/10.13039/501100011033/FEDER, UE, NextGenerationEU/PRT. M.A-F. acknowledges support from the Emergia program (EMERGIA20-38888) from Consejería de Universidad, Investigación e Innovación de la Junta de Andalucía. JR acknowledges funding from University of La Laguna through the Margarita Salas Program from the Spanish Ministry of Universities ref. UNI/551/2021-May 26, and under the EU Next Generation. BB acknowledges financial from the Grant AST22_4.4, funded by Consejería de Universidad, Investigación e Innovación and Gobierno de España and Unión Europea – NextGenerationEU, and by the research project PID2020-113689GB-I00 financed by MCIN/AEI/10.13039/501100011033. GTR acknowledges financial support from the research project PRE2021-098736, funded by MCIN/AEI/10.13039/501100011033 and FSE+. This research made use of astropy, a community-developed core python (<http://www.python.org>) package for Astronomy (Astropy Collaboration 2013); ipython (Pérez & Granger 2007); matplotlib (Hunter 2007); numpy (Walt et al. 2011); scipy (Jones et al. 2001); and topcat (Taylor 2005). This research has made use of the NASA/IPAC Extragalactic Database, operated by the Jet Propulsion Laboratory of the California Institute of Technology, under contract with the National Aeronautics and Space Administration. Funding for SDSS-III has been provided by the Alfred P. Sloan Foundation, the Participating Institutions, the National Science Foundation, and the U.S. Department of Energy Office of Science. The SDSS-III Web site is <http://www.sdss3.org/>. The SDSS-IV site is <http://www.sdss.org>. This publication was based on observations collected under the CAVITY legacy project.

References

- Abazajian, K. N., Adelman-McCarthy, J. K., & Agüeros. 2009, *ApJS*, 182, 543
 Ahumada, R., Allende Prieto, C., Almeida, A., et al. 2020, *ApJS*, 249, 3
 Akhlaghi, M. & Ichikawa, T. 2015, *ApJS*, 220, 1
 Argudo-Fernández, M., Duarte Puertas, S., Ruiz, J. E., et al. 2017, *PASP*, 129, 058005
 Argudo-Fernández, M., Verley, S., Bergond, G., et al. 2015, *A&A*, 578, A110
 Astropy Collaboration, Price-Whelan, A. M., Sipőcz, B. M., et al. 2018, *AJ*, 156, 123
 Astropy Collaboration, Robitaille, T. P., Tollerud, E. J., et al. 2013, *A&A*, 558, A33
 Behnel, S., Bradshaw, R., Citro, C., et al. 2011, *Computing in Science & Engineering*, 13, 31
 Bertin, E. 2006, in *Astronomical Society of the Pacific Conference Series*, Vol. 351, *Astronomical Data Analysis Software and Systems XV*, ed. C. Gabriel, C. Arviset, D. Ponz, & S. Enrique, 112
 Bertin, E. & Arnouts, S. 1996a, *A&AS*, 117, 393
 Bertin, E. & Arnouts, S. 1996b, *A&AS*, 117, 393
 Beygu, B., Kreckel, K., van der Hulst, J. M., et al. 2016, *MNRAS*, 458, 394
 Beygu, B., Peletier, R. F., van der Hulst, J. M., et al. 2017, *MNRAS*, 464, 666
 Brassington, N. J., Zezas, A., Ashby, M. L. N., et al. 2015, *ApJS*, 218, 6
 Bundy, K., Bershad, M. A., Law, D. R., et al. 2015, *ApJ*, 798, 7
 Cappellari, M. & Copin, Y. 2003, *MNRAS*, 342, 345
 Cappellari, M. & Emsellem, E. 2004, *PASP*, 116, 138
 Cardelli, J. A., Clayton, G. C., & Mathis, J. S. 1989, *ApJ*, 345, 245
 Cautun, M., van de Weygaert, R., Jones, B. J. T., & Frenk, C. S. 2014, *MNRAS*, 441, 2923
 Cid Fernandes, R., Pérez, E., García Benito, R., et al. 2013, *A&A*, 557, A86
 Colberg, J. M., Pearce, F., Foster, C., et al. 2008, *MNRAS*, 387, 933
 Constantin, A., Hoyle, F., & Vogeley, M. S. 2008, *ApJ*, 673, 715
 Debattista, V. P., Mayer, L., Carollo, C. M., et al. 2006, *ApJ*, 645, 209
 Dekel, A. & Cox, T. J. 2006, *MNRAS*, 370, 1445
 del Moral-Castro, I., García-Lorenzo, B., Ramos Almeida, C., et al. 2019, *MNRAS*, 485, 3794
 del Moral-Castro, I., García-Lorenzo, B., Ramos Almeida, C., et al. 2020, *A&A*, 639, L9
 Dey, A., Schlegel, D. J., Lang, D., et al. 2019, *AJ*, 157, 168
 Di Matteo, T., Springel, V., & Hernquist, L. 2005, *Nature*, 433, 604
 Domínguez-Gómez, J., Lisenfeld, U., Pérez, I., et al. 2022, *A&A*, 658, A124
 Domínguez-Gómez, J., Pérez, I., Ruiz-Lara, T., et al. 2023a, *arXiv e-prints*, arXiv:2310.11412
 Domínguez-Gómez, J., Pérez, I., Ruiz-Lara, T., et al. 2023b, *Nature*, 619, 269
 Douglass, K. A., Smith, J. A., & Demina, R. 2019, *ApJ*, 886, 153
 Douglass, K. A., Veyrat, D., & BenZvi, S. 2022, *arXiv e-prints*, arXiv:2202.01226
 Dressler, A. 1980, *ApJ*, 236, 351
 El-Ad, H. & Piran, T. 1997, *ApJ*, 491, 421
 Falcón-Barroso, J., Bacon, R., Bureau, M., et al. 2006, *MNRAS*, 369, 529
 Falcón-Barroso, J., Sánchez-Blázquez, P., Vazdekis, A., et al. 2011, *A&A*, 532, A95
 Falcón-Barroso, J., van de Ven, G., Lyubenova, M., et al. 2019, *A&A*, 632, A59
 García-Benito, R., González Delgado, R. M., Pérez, E., et al. 2017, *A&A*, 608, A27
 García-Benito, R. & Pérez-Montero, E. 2012, *MNRAS*, 423, 406
 Hopkins, P. F., Somerville, R. S., Hernquist, L., et al. 2006, *ApJ*, 652, 864
 Hoyle, F. & Vogeley, M. S. 2002, *ApJ*, 566, 641
 Hoyle, F. & Vogeley, M. S. 2004, *ApJ*, 607, 751
 Husemann, B., Jahnke, K., Sánchez, S. F., et al. 2013, *A&A*, 549, A87
 Husemann, B., Kamann, S., Sandin, C., et al. 2012, *A&A*, 545, A137
 Jedrzejewski, R. I. 1987, *MNRAS*, 226, 747
 Kelz, A., Verheijen, M. A. W., Roth, M. M., et al. 2006, *PASP*, 118, 129
 Klypin, A., Valenzuela, O., Colín, P., & Quinn, T. 2009, *MNRAS*, 398, 1027
 Knapen, J. H. & Cisternas, M. 2015, *ApJ*, 807, L16
 Kreckel, K., Croxall, K., Groves, B., van de Weygaert, R., & Pogge, R. W. 2015, *ApJ*, 798, L15
 Kroupa, P. 2001, *MNRAS*, 322, 231
 Lacerda, E. A. D., Sánchez, S. F., Mejía-Narváez, A., et al. 2022, *New A*, 97, 101895
 Lackner, C. N., Cen, R., Ostriker, J. P., & Joung, M. R. 2012, *MNRAS*, 425, 641
 Lang, D., Hogg, D. W., Mierle, K., Blanton, M., & Roweis, S. 2010, *AJ*, 139, 1782
 Larson, R. B. & Tinsley, B. M. 1978, *ApJ*, 219, 46
 Libeskind, N. I., van de Weygaert, R., Cautun, M., et al. 2018, *MNRAS*, 473, 1195
 Maiolino, R., Gallerani, S., Neri, R., et al. 2012, *MNRAS*, 425, L66
 Makarov, D., Prugniel, P., Terekhova, N., Courtois, H., & Vauglin, I. 2014, *A&A*, 570, A13
 Marino, R. A., Rosales-Ortega, F. F., Sánchez, S. F., et al. 2013, *A&A*, 559, A114
 Moster, B. P., Naab, T., & White, S. D. M. 2013, *MNRAS*, 428, 3121

- Nadathur, S. & Hotchkiss, S. 2014, *MNRAS*, 440, 1248
- Neyrinck, M. C. 2008, *MNRAS*, 386, 2101
- Nikolic, B., Cullen, H., & Alexander, P. 2004, *MNRAS*, 355, 874
- Pan, D. C., Vogeley, M. S., Hoyle, F., Choi, Y.-Y., & Park, C. 2012, *MNRAS*, 421, 926
- Park, C., Choi, Y.-Y., Vogeley, M. S., et al. 2007, *ApJ*, 658, 898
- Pérez, I., Martínez-Valpuesta, I., Ruiz-Lara, T., et al. 2017, *MNRAS*, 470, L122
- Pietrinferni, A., Cassisi, S., Salaris, M., & Castelli, F. 2004, *ApJ*, 612, 168
- Platen, E., van de Weygaert, R., & Jones, B. J. T. 2008, *MNRAS*, 387, 128
- Pohlen, M. & Trujillo, I. 2006, *A&A*, 454, 759
- Pustilnik, S. A. & Tepliakova, A. L. 2011, *MNRAS*, 415, 1188
- Quilis, V., Moore, B., & Bower, R. 2000, *Science*, 288, 1617
- Rojas, R. R., Vogeley, M. S., Hoyle, F., & Brinkmann, J. 2004, *ApJ*, 617, 50
- Rojas, R. R., Vogeley, M. S., Hoyle, F., & Brinkmann, J. 2005, *ApJ*, 624, 571
- Román, J., Rich, R. M., Ahvazi, N., et al. 2023, *A&A*, 679, A157
- Román, J., Trujillo, I., & Montes, M. 2020, *A&A*, 644, A42
- Roth, M. M., Kelz, A., Fechner, T., et al. 2005, *PASP*, 117, 620
- Roškar, R., Debattista, V. P., Stinson, G. S., et al. 2008, *ApJ*, 675, L65
- Ruiz-Lara, T., Beasley, M. A., Falcón-Barroso, J., et al. 2018a, *MNRAS*, 478, 2034
- Ruiz-Lara, T., Gallart, C., Beasley, M., et al. 2018b, *A&A*, 617, A18
- Ruiz-Lara, T., Pérez, I., Florido, E., et al. 2016, *MNRAS*, 456, L35
- Ruiz-Lara, T., Pérez, I., Gallart, C., et al. 2015, *A&A*, 583, A60
- Sánchez, S. F., Aceituno, J., Thiele, U., Pérez-Ramírez, D., & Alves, J. 2007, *PASP*, 119, 1186
- Sánchez, S. F., García-Benito, R., Zibetti, S., et al. 2016a, *A&A*, 594, A36
- Sánchez, S. F., Kennicutt, R. C., Gil de Paz, A., et al. 2012, *A&A*, 538, A8
- Sánchez, S. F., Pérez, E., Sánchez-Blázquez, P., et al. 2016b, *Rev. Mexicana Astron. Astrofis.*, 52, 171
- Sánchez, S. F., Pérez, E., Sánchez-Blázquez, P., et al. 2016c, *Rev. Mexicana Astron. Astrofis.*, 52, 21
- Sánchez-Alarcón, P. M., Román, J., Knapen, J. H., et al. 2023, *A&A*, 677, A117
- Sánchez-Blázquez, P., Courty, S., Gibson, B. K., & Brook, C. B. 2009, *MNRAS*, 398, 591
- Sánchez-Blázquez, P., Peletier, R. F., Jiménez-Vicente, J., et al. 2006, *MNRAS*, 371, 703
- Sánchez-Blázquez, P., Rosales-Ortega, F. F., Méndez-Abreu, J., et al. 2014, *A&A*, 570, A6
- Sarzi, M., Falcón-Barroso, J., Davies, R. L., et al. 2006, *MNRAS*, 366, 1151
- Scudder, J. M., Ellison, S. L., Torrey, P., Patton, D. R., & Mendel, J. T. 2012, *MNRAS*, 426, 549
- Seidel, M. K., Falcón-Barroso, J., Martínez-Valpuesta, I., et al. 2015, *MNRAS*, 451, 936
- Simon, J. D. & Geha, M. 2007, *ApJ*, 670, 313
- Stanonik, K., Platen, E., Aragón-Calvo, M. A., et al. 2009, *ApJ*, 696, L6
- Sutter, P. M., Lavaux, G., Hamaus, N., et al. 2015, *Astronomy and Computing*, 9, 1
- Tempel, E., Tuvikene, T., Kipper, R., & Libeskind, N. I. 2017, *A&A*, 602, A100
- van de Weygaert, R., Kreckel, K., Platen, E., et al. 2011, in *Astrophysics and Space Science Proceedings*, Vol. 27, Environment and the Formation of Galaxies: 30 years later, 17
- van de Weygaert, R. & Platen, E. 2011, in *International Journal of Modern Physics Conference Series*, Vol. 1, International Journal of Modern Physics Conference Series, 41–66
- Vazdekis, A., Coelho, P., Cassisi, S., et al. 2015, *MNRAS*, 449, 1177
- Vazdekis, A., Koleva, M., Ricciardelli, E., Röck, B., & Falcón-Barroso, J. 2016, *MNRAS*, 463, 3409
- Watkins, A. E., Kaviraj, S., Collins, C. C., et al. 2024, *MNRAS*, 528, 4289
- Zernike, F. 1934, *MNRAS*, 94, 377
- Zhang, J., Martin, P. G., Cloutier, R., et al. 2023, *ApJ*, 948, 4
- ⁷ Departamento de Astrofísica, Universidad de La Laguna, 38200 La Laguna, Tenerife, Spain
- ⁸ Universidad Nacional Autónoma de México, Instituto de Astronomía, AP 106, Ensenada 22800, BC, México
- ⁹ Department of Physics and Astronomy, University of British Columbia, Vancouver, BC V6T 1Z1, Canada
- ¹⁰ Instituto de Astrofísica, Facultad de Física, Pontificia Universidad Católica de Chile, Av. Vicuña Mackenna 4860, Santiago, Chile
- ¹¹ Instituto de Astronomía, Universidad Nacional Autónoma de México, A. P. 70-264, 04510, México, D.F., Mexico
- ¹² Departament d’Astronomia i Astrofísica, Universitat de València, E-46100 Burjassot (València), Spain
- ¹³ Bernoulli Institute for Mathematics, Computer Science and Artificial Intelligence, University of Groningen, 9700 AK, Groningen, The Netherlands
- ¹⁴ Astronomisches Rechen-Institut, Zentrum für Astronomie der Universität Heidelberg, 69120 Heidelberg, Germany
- ¹⁵ Université Claude Bernard Lyon 1, IUF, IP2I Lyon, 4 rue Enrico Fermi, Villeurbanne, 69622, France
- ¹⁶ ICE-CSIC, Carrer de Can Magrans, 08193 Cerdanyola del Vallés, Barcelona, Spain
- ¹⁷ Departamento de Física de la Tierra y Astrofísica & IPARCOS, Universidad Complutense de Madrid, E-28040, Madrid, Spain
- ¹⁸ Institut de Radioastronomie Millimétrique (IRAM), Av. Divina Pastora 7, Local 20, 18012 Granada, Spain
- ¹⁹ School of Physics and Astronomy, Univ. of St Andrews, North Haugh, St Andrews, KY16 9SS, UK
- ²⁰ Centro Astronómico Hispano en Andalucía, Observatorio de Calar Alto, Sierra de los Filabres, 04550 Gérgal, Almería, Spain

¹ Universidad de Granada, Departamento de Física Teórica y del Cosmos, Campus Fuentenueva, Edificio Mecenaz, E-18071, Granada, Spain. e-mail: isa@ugr.es

² Instituto Carlos I de Física Teórica y Computacional, Facultad de Ciencias, E-18071 Granada, Spain

³ Instituto de Astrofísica de Andalucía - CSIC, Glorieta de la Astronomía s.n., 18008 Granada, Spain

⁴ Département de Physique, de Génie Physique et d’Optique, Université Laval, and Centre de Recherche en Astrophysique du Québec (CRAQ), Québec, QC, G1V 0A6, Canada

⁵ Kapteyn Astronomical Institute, University of Groningen, Landleven 12, 9747 AD Groningen, The Netherlands

⁶ Instituto de Astrofísica de Canarias, Vía Láctea s/n, 38205 La Laguna, Tenerife, Spain

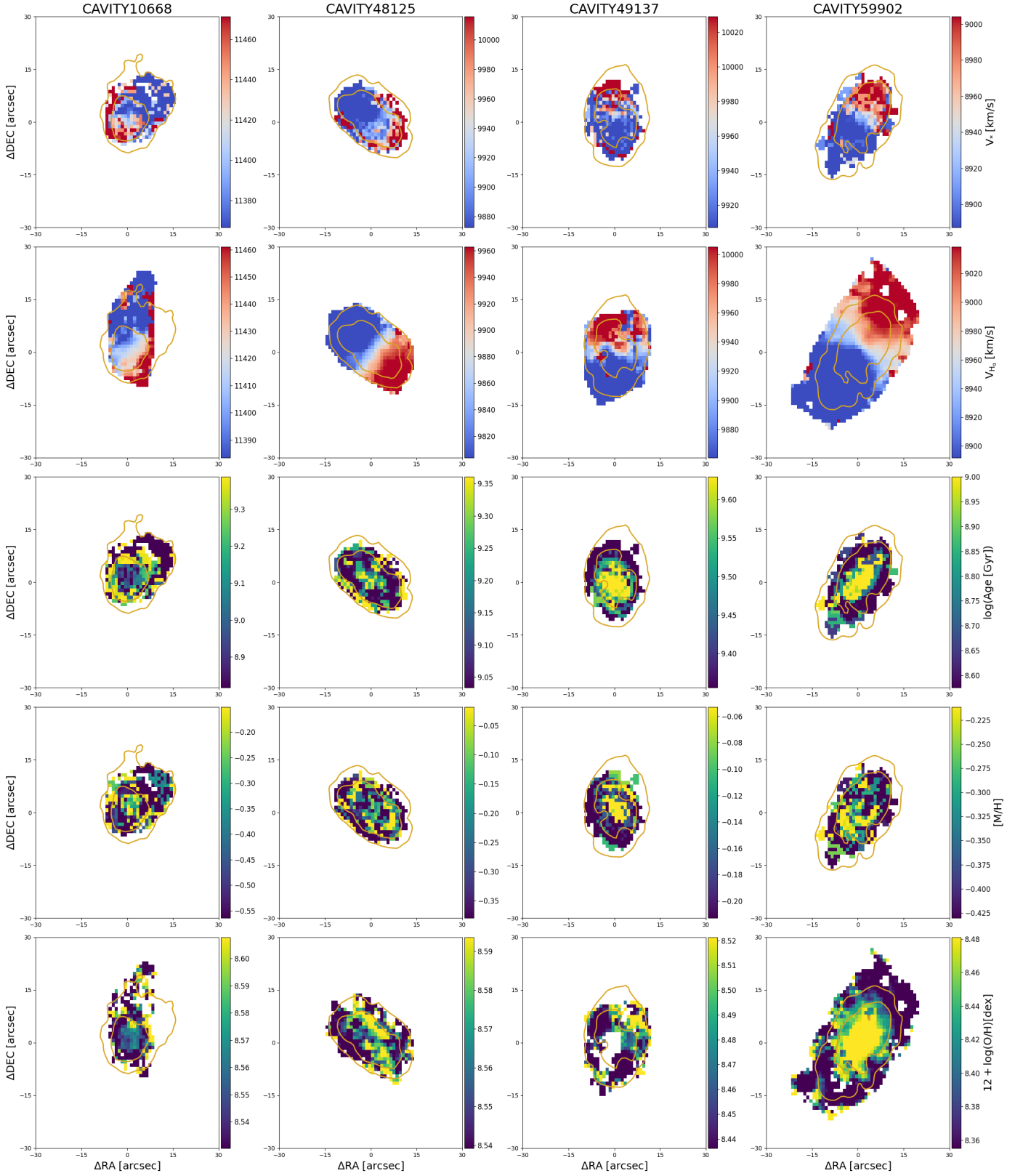


Fig. 8. Typical science products that we can obtain from the CAVITY IFS cubes. From left to right we show maps for galaxies CAVITY10668, CAVITY48125, CAVITY49137, and CAVITY59902. From top to bottom we show maps of stellar velocity, $H\alpha$ velocity, stellar age (log-scale, light-weighted), stellar metallicity (light-weighted $[Z/H]$), and gas abundance ($12 + \log(O/H)$). Contours corresponding to a SNR level of 10 and 30 are overlotted.

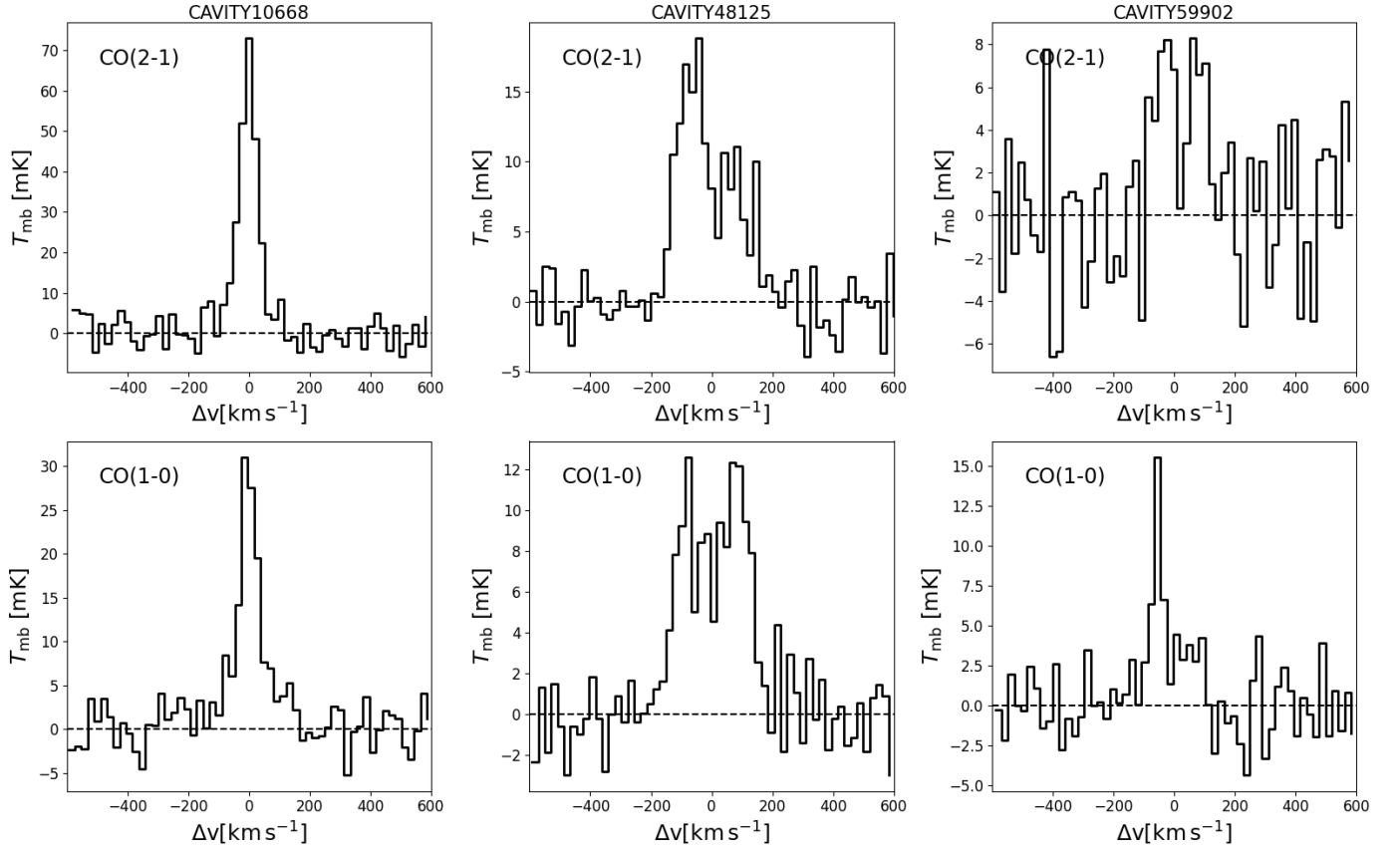


Fig. 9. CO(2-1) (top) and CO(1-0) (bottom) spectra from our IRAM observations for CAVITY10668, CAVITY48125, and CAVITY59902 (from left to right).

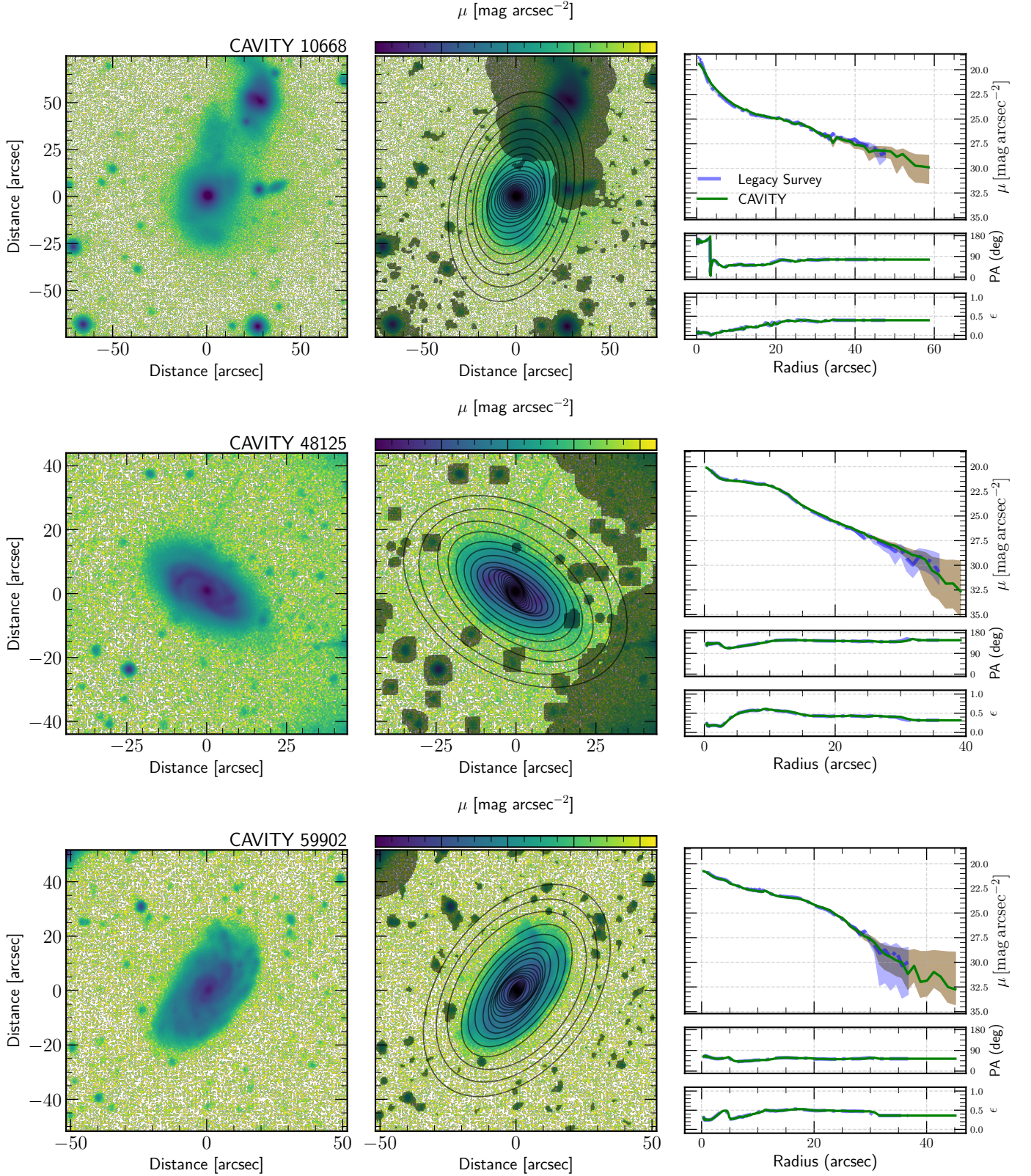


Fig. 10. Analysis of the light distribution from the INT deep imaging campaigns for the three galaxies included in this paper with INT data so far (CAVITY10668, CAVITY48125, and CAVITY59902, from top to bottom). Left-hand panels show the g-band images from the INT campaign. Middle panels display, on top of the INT images, the masking scheme as well as the isophotal ellipses with varying ellipticity and position angle. Right-hand panels show profiles of SB, position angle (PA) and ellipticity (ϵ) for the three galaxies under analysis. Green lines correspond to the profiles from the INT images. Blue, dashed lines are obtained from DECALS using the same procedure as for the INT images. See text for details.

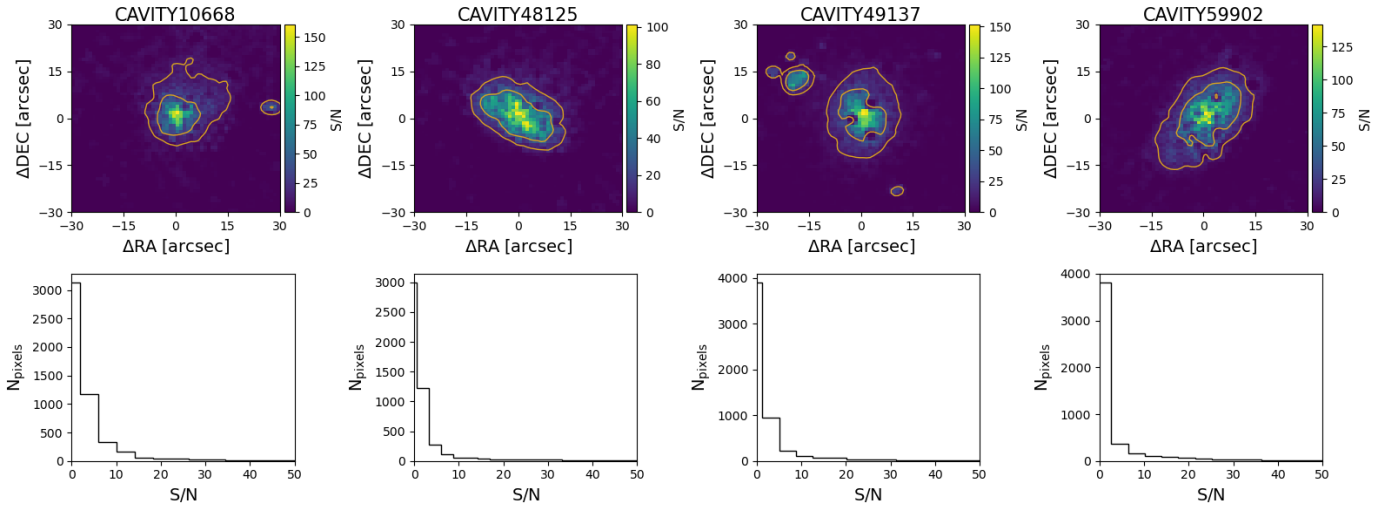


Fig. 11. Assessment of the quality of the datacubes of the four CAVITY galaxies under analysis. Top panels: Continuum SNR maps. Contours correspond to a SNR level of 10 and 30, respectively. Bottom panels: Continuum SNR histograms.